

PREPRINT FROM

**LOS ALAMOS SCIENTIFIC LABORATORY**  
of the  
**University of California**  
LOS ALAMOS • NEW MEXICO

ELASTIC SCATTERING OF FAST NEUTRONS BY LIQUID HYDROGEN,  
DEUTERIUM, TRITIUM AND BY He<sup>3</sup>

By

John D. Seagrave



UNITED STATES  
ATOMIC ENERGY COMMISSION  
CONTRACT W-7405-ENG. 36

000235

Abstract for invited paper to be presented at the Symposium on Light Nuclei, Few Body Problems and Nuclear Forces at Brela, Yugoslavia, 26 June - 5 July, 1967 by John D. Seagrave, Los Alamos Scientific Laboratory, Los Alamos, New Mexico.

Elastic Scattering of Fast Neutrons by Liquid Hydrogen,  
Deuterium, Tritium and by He<sup>3</sup>\*

John D. Seagrave  
Los Alamos Scientific Laboratory, Los Alamos, New Mexico

ABSTRACT

Over the past two years, an extensive program at the LASL "Buncher" fast-neutron time-of-flight facility has been devoted to the study of elastic scattering of fast neutrons of energies between 5.6 and 23 MeV by all three hydrogen isotopes, in liquid form. A thin-walled cryostat system was developed, capable of providing a cylindrical sample containing one mole of T<sub>2</sub> in liquid form; the cryostat is described together with its associated mobile gas-handling system. By the use of an identical sample cell and cryostat filled with liquid hydrogen, calibration points were obtained at angles chosen to give scattered neutron energies corresponding to deuterium or tritium data points, in an overlapping network of data points at the different incident neutron energies. Improved techniques for collimation of fast neutrons, which were developed concurrently, are also illustrated.

Recent data on the total, elastic, and non-elastic cross sections for the three hydrogen isotopes and for He<sup>3</sup> are surveyed. New elastic angular distributions for n-D scattering at 9 energies and for n-T scattering at 6 energies between 5.6 and 23 MeV are presented together with results of other experiments, and with data for charge-conjugate p-D and p-He<sup>3</sup> scattering, as

---

\* Work performed under the auspices of the U.S. Atomic Energy Commission.

families of differential cross sections plotted against the cosine of the c.m. scattered-particle angle, displaced along oblique energy axes. In a similar manner, available polarization data is examined, though no new polarization data is contributed. An analogous review of n-He<sup>3</sup> and p-T elastic scattering and polarization data is provided, which includes unpublished p-T elastic data at 14.6 MeV of Leland and Rosen at LASL. Wick's Limit (or the Optical Theorem) is discussed as a guide to data evaluations and illustrated on these charts. A composite graph of LASL, LRL, and Wisconsin T(p,n)He<sup>3</sup> angular distributions is shown together with the corresponding curves for He<sup>3</sup>(n,p)T calculated from the Detailed Balance relation.

For use in multiple-scattering and attenuation calculations by a Monte Carlo method, phase-space calculations were made for the energy and angular distributions expected on that basis for D(n,2n), T(n,2n) and T(n,3n) neutrons over the range of incident energies from threshold to 23 MeV, normalized to known or estimated non-elastic cross sections. Curves of these results are shown, and compared to Zagreb D(n,p)2n data at 14.4 MeV. D(p,2p) distributions are also compared with available data at 13.9 MeV, and both sets are in reasonable agreement with the data, apart from the much-studied forward-peaked final-state interaction.

Plans for polarization measurements related to the recent elastic scattering measurements are outlined, and a description is given of the multi-purpose klystron-type pulsed ion source soon to be installed on the LASL Tandem accelerator---in addition to the Polarized Ion Source described earlier at this Symposium.

The experimental work described in this paper was performed in collaboration with John C. Hopkins and P.W. Keaton of the LASL Physics Division and Robert H. Sherman and Eugene C. Kerr of the LASL Cryogenics Group.

## INTRODUCTION

The Physics Division of the Los Alamos Scientific Laboratory has had a very active interest, since its inception, in the investigation of the interactions of what have come to be called "few-nucleon" systems. To establish a perspective for the new work to be reviewed, let me remind you briefly of some of the fast-neutron aspects of this program with which I have been involved. When I first came to Los Alamos in 1951, a special meter-long transmission cell for total cross-section measurements of gaseous elements had been developed and was being used for the measurements on hydrogen and tritium,  $\text{He}^3$  and  $\text{He}^4$ , subsequently published [1] under the authorship of "The Los Alamos Physics and Cryogenic Groups." The project had indeed involved nearly everyone in both groups. As a newcomer, my contribution was to sit on the lid of a large "safety" storage can for the cell and capillary tubing containing  $\text{T}_2$  gas at over 100 atmospheres until a pump evacuated the volume surrounding the cell and the gasket was compressed sufficiently to permit locking down the lid. The cell was subsequently used for a similar series of measurements on  $\text{D}_2$  gas [2]. Angular distributions for n- $\text{He}^4$  scattering [3] were undertaken with a recoil proportional counter, and for n-D scattering with a counter telescope [4] at 14 MeV using deuterated polyethylene ( $\text{CD}_2$ ) foils, and later with Cranberg's time-of-flight system using solid  $\text{CD}_2$  cylinders [5]. For further angular distribution measurements, we made a spherical scattering sample to contain  $\text{He}^3$  at 350 atmospheres. We could find no volunteers to sit on that one if filled with  $\text{T}_2$ , so a thin-walled spherical cell was prepared to hold about 0.5 atomic moles of tritium in the form of  $\text{CaT}_2$ , and contain the expected  $1 \text{ cm}^3$  of  $\text{He}^3$  evolved per day.

With these samples, differential cross sections were measured at 1, 2, 3.5, and 6 MeV for  $\text{He}^3$  and tritium [6], and reported at the London Few-Nucleon Conference in 1959 [7]. In another paper at that Conference [8], LASL work by Perry, et al. on the  $\text{T}(p,n)\text{He}^3$  was evaluated and the cross sections for the inverse reaction calculated by the principle of Detailed Balance. I mention this bibliography of related earlier work because one aspect or another of each item has come up in preparation for this review. We may examine in

FIG. 1, which shows them on a log-log scale in a manner reminiscent of the old-style Brookhaven "wallpaper books" [9], the total and non-elastic cross sections for fast-neutron interaction with the three hydrogen isotopes: H, D, and T over the energy range between 0.1 and 30 MeV. The hydrogen total cross section needs little comment, and has recently been reviewed by Horsley [10] in the range up to 20 MeV, and by Schmidt [11] at Karlsruhe in the range up to 10 MeV. Reference should be made to several recent measurements of unprecedented precision, at Columbia [12,13], which we have already considered [14], and at Canberra [15]. The tritium total cross section measurements shown come entirely from the LASL series of measurements [1], concerning which I have already remarked on my quite sedentary part. The four small open circles are the elastic integrals of our differential cross section data at 1, 2, 3.5, and 6 MeV [6]. The deuterium total cross section has received much wider attention. The open circles are our measurements with the same meter-long transmission cell [2], the open [16] and solid [17] diamonds are measurements at LRL,\* and the cluster of solid circles are measurements at ORNL [18] designed to test a hypothesis [19] of a possible anomaly near

---

\*Additional data of Ref. 17 above 21 MeV, of Riddle at AERE [23], and several points near 14 MeV [24-26] are not shown.

the threshold of  $D(n,2n)P$  breakup at 3.35 MeV. No such anomaly was found. The additional low-energy points are integrals of several elastic angular distributions, some of which have been shown earlier [22]. The curve is drawn toward the empirical zero-energy value  $3.2 \pm 0.1$  barns which we have already discussed [22]. Turning to the non-elastic cross sections, the Livermore [27] measurements of the  $D(n,2n)P$  cross section, integrated in a liquid-scintillator tank, are shown with extrapolations which look reasonable on both log-log and linear plots. The behavior near threshold is unknown. The  $T(n,2n)D$  cross section has been suspected of being rather smaller than the  $D(n,2n)P$  case for some time, contrary to earlier estimates [28]. Several  $n-T$  elastic cross section estimates based on  $p\text{-He}^3$  measurements and the total cross section [29] give values in the range indicated by the shaded bars. This has been confirmed by scintillator-tank measurements by Mather and Pain at AWRE [30], who report values at 14.1 MeV for  $T(n,2n)D$  and  $T(n,3n)P$  of  $45 \pm 5$  and  $0 \pm 1$  mb, respectively. These values were obtained using a yttrium tritide sample, in the presence of a  $Y(n,2n)$  cross section of  $900 \pm 45$  mb.

#### LIQUID SAMPLES OF THE HYDROGEN ISOTOPES

It became clear several years ago that interest in continuing measurements on these systems, and the advance of cryogenic techniques suggested that a sample suitable for fast-neutron scattering measurements on the liquid hydrogen isotopes, including tritium, could be designed. Liquid tritium ( $LT_2$ ) has a molal volume of about  $23 \text{ cm}^3/\text{mole}$ , and although one mole (6 grams) of tritium experiences 1.8 watts of  $\beta$ -decay radiation heating, it was felt that a cylindrical sample containing one mole could be handled using only conduction cooling by liquid hydrogen ( $LH_2$ ), in view of the marked isotope effect seen in

FIG. 2, which gives the transition temperatures of the hydrogen isotopes, represented as bar-graphs in a form intended to suggest thermometers. The boiling points are given for standard atmospheric pressure at the right, and it may be noted that there is a  $4.5^{\circ}\text{K}$  difference between the values for tritium and hydrogen. At the altitude of Los Alamos (2.2 km), the average barometric pressure is only about 600 mm (Torr), and the corresponding temperatures are depressed  $0.8$  or  $0.9^{\circ}\text{K}$  as shown in the bar-graph at the left. The center graph shows the triple points, which are the temperatures corresponding to melting on warming up from a condition frozen in a vacuum, that is, developing their own vapor pressure in a closed system. The chart shows that there is a possibility of freezing  $\text{LT}_2$  if the coolant  $\text{LH}_2$  were allowed to boil freely to the atmosphere at Los Alamos, so the system envisioned provided for manipulating the temperature through control of the hydrogen coolant pressure by a pressure regulator ahead of the vent. In the same manner, a  $\text{LH}_2$  sample could be kept in a cell in thermal contact with refrigerant  $\text{LH}_2$  at a different pressure. The sample-cryostat developed is shown in

FIG. 3. The upper portion is a 6-liter dewar reservoir of  $\text{LH}_2$ , connected to a thin tube closed at the top of the cell. The  $\text{LH}_2$  thus extends the full length of two smaller coaxial tubes which connect the gas-handling system with the cell. The scale will be clearer in subsequent photographs, but the inner cell tip is 4.1 cm long and 2.7 cm in diameter ( $23.49 \text{ cm}^3$  volume), with 0.0075-cm walls and 0.05-cm end, machined from solid stainless steel.\* The cell and dewar are surrounded by an insulating vacuum maintained by a triode appendage ion pump. The outer tip has a thickness of 0.01 cm. In the system of three coaxial tubes, the middle wall is in contact with  $\text{LH}_2$  from the dewar, and gas admitted in contact with its inner surface condenses

---

\* Dimensions shown on the drawing are in mils ( $1 \text{ mm} \approx 40$  milli-inches).

and flows into the cell. To preclude violent surging as in a coffee percolator, the inmost tube provides for venting the cell as liquid flows in, and for  $T_2$  vapor recycling and  $He^3$  venting. An X-ray of the cell is shown as SLIDE 3A\*, which may serve to clarify the assembly of this delicate piece of hardware. The inner tubes are readily seen. The  $LH_2$  coolant region terminates well above the cell but the latter was overfilled to insure good thermal transfer, and a constant volume visible to the neutron detector. To permit use of the cryostat with tritium, which requires a closed system, we envisioned a mobile gas-handling system with supplies of  $H_2$ ,  $D_2$ , and  $T_2$  gas, helium for line-flushing, and a 50-liter supply dewar of  $LH_2$ , with two identical sample cells and the associated dewars mounted from a boom, as in

FIG. 4, which shows this scheme. The forward cell would always be filled with  $LH_2$  for detector sensitivity calibration (discussed later), and an identical dummy cell tip with about 30 cm of the cryostat "tail" would be provided for background measurements. It took most of two years to get this concept implemented and ready for tritium, counting preliminary operating experience with  $LD_2$ . I have four color slides of this apparatus.

SLIDE 4A gives a view of the control panel for gauges and valves, which mercifully hides the frightening maze of plumbing, all color-coded to correspond to the valves and a colored master diagram. You may be relieved to hear that I do not plan to inflict you with a slide of that diagram, colorful though it is! SLIDE 4B shows the two cryostats supported on a boom, or "bowsprit" extending forward of the mobile system we called the "Chariot." The inner, or  $LT_2$  cell is in position in front of the gas target neutron source, stabilized in a groove in a bracket by rubber bands. Also

---

\* Illustrations referred to as "slides" in text are unsuitable for reproduction in the Proceedings, and are included as supplementary to the line drawings referred to as "figures."

visible are the  $T_2$  supply tanks, the shadow cone and front collimator which I will discuss shortly, and the time-of-flight neutron source monitor overhead at an angle of about  $110^\circ$  to the beam axis. The front  $LH_2$  cell is protected by a colored plastic sleeve. SLIDE 4C shows a closer view of the target, sample, bracket, monitor tip, and front collimator, as well as the cooling spray for the target, and the dummy cell hanging to one side (also covered with a protective colored plastic sleeve). Finally, SLIDE 4D shows the complete apparatus. One may see an overhead rail system to constrain the top-heavy Chariot, which has a worm-gear front-wheel drive, and a pair of roller-chain-coupled swivelling rear wheels. Driving it into sample position is rather like docking an outboard-motor boat in a heavy current. The detector shield and collimator system seen at the right is mounted on a rail system which permits change of flight path length, and which is pivoted under the scattering sample and driven about in angle by two large tires on a rigid track at about five meters radius. At forward angles, it was necessary to pass the front  $LH_2$  cell through a gap between the front and main collimators.

#### NEUTRON COLLIMATOR DESIGN

In planning to extend operations with the LASL "Buncher" time-of-flight system into the fast-neutron region up to 23 MeV, it was clear that a completely new collimator and shield system would be required, as the former borated-paraffin shields would be relatively transparent at the higher energies. Tungsten and copper are outstanding for high-energy neutron shielding. Since the very large cross sections for forward scattering by the heavy metals means that the elastic cross section can be neglected in its

effect on shielding, one may estimate the usefulness of such materials on the basis of their non-elastic cross sections, providing the resulting degraded low-energy neutrons can be handled, and the resulting gamma flux is not objectionable. Since we planned to deal with gammas by pulse-shape discrimination, using NE 213 liquid scintillator,\* there was also no point in retaining the usual  $B^{10}$  loading of hydrogenous material, designed to absorb thermalized neutrons and prevent generation of gammas by the  $H(n,\gamma)D$  capture process.

FIG. 5 gives the non-elastic absorption coefficient, defined as shown on the graph, for these materials, and also for iron and lead, in units of inverse centimeters. Also shown is the analogous attenuation coefficient for hydrogen, assumed present in the form of  $CH_2$ , based on the total cross section. The reasonably flat value for tungsten over the range of interest is about  $0.17 \text{ cm}^{-1}$ , where data is available. This corresponds to roughly a factor of two absorption in 5 cm. However, where weight is a factor, copper, which is 2.17 times less dense than tungsten, is superior above about 2 MeV. We happened to have a number of disks of a "machineable" tungsten alloy and a large collection of 1.3-cm square bars of elemental tungsten, so we adapted the disks to the cylindrical front collimator already shown in the photographs, and glued up the bars into slabs with which to make a rectangular-aperture collimator throat to be described shortly. Another technique which becomes increasingly important as neutron energy increases is the handling of the front shadow bar or cone. In

FIG. 6 we see its use schematically illustrated. One wishes to place as much attenuating material as possible between the source and the detector along paths D and E, and also to shield the front end of the

---

\* NE 213 is manufactured by Nuclear Enterprises, Inc.

collimator along line C to minimize in-scattering of primary neutrons. At the same time, one must avoid interposing material between the source and sample (line A) or between sample and detector (line B). These requirements are of course somewhat mutually exclusive, and their relative importance will vary with energy and angle. The positioning must also be quite reproducible if it is necessary to remove the shadow bar for mechanical reasons between sample and background runs. To better control these variables, we [31] have developed a linkage system which constrains the tip of the shadow cone to follow line A, and the flat side to follow line B as the entire collimator system is rotated. This arrangement is sketched in FIG. 7. When the main collimator track is rotated, the channel attached to the front collimator pivots about a bearing directly below the scattering sample, pushing the plate on which the shadow cone rides (through the bearings inside the channel) and the plate is thus constrained to slide along line B; at the same time, a bearing directly under the tip of the cone moves in a slot in the support plate which represents the constraint along the line A. Both constraints are separately adjustable to permit optimizing conditions empirically. The throat of the main collimator is made of glued-up slabs of tungsten 2.6 cm thick assembled in such a manner that the prismatic throat can readily be adjusted to match any reasonable combination of flight distance and sample size. This is shown in

FIG. 8: Slab 1 lies horizontal on a shelf of the main collimator, and slab 2 is butted against it in a vertical plane inclined to the axis of symmetry so as to define the left side of the prism. Slab 3 hangs underneath a moveable shelf of the assembly and is both cocked to the left and upward at the rear to define the top side of the prism. Slab 4 is a rectangular bar inclined toward the axis, opposite to slab 2, but fitting under the overhanging

slab 3. The remaining gap is closed by piece 5, which is a wedge (the angles are so small that the top surface may be taken perpendicular to the sides without leaving an appreciable crack). After assembly, the outside is packed with additional copper bars as may seem necessary, and the rest of the shelves loaded with sheets of  $\text{CH}_2$ . Compare Figs. 9 and 10. Two photomultipliers viewed a liquid scintillator 5 cm thick by 12 cm diameter, a 56AVP adjusted for best timing, and a 58AVP for linear and neutron-gamma discrimination signals.

To show how all this hardware fits together with the Buncher facility,

FIG. 9 has been prepared to give a schematic plan view of the system.

A deuteron beam from the LASL Vertical Van de Graaff accelerator is chopped in the high-voltage terminal into bursts of about 10 nanoseconds (ns) duration at a 2 MHz rate, and then passed between deflector plates operating at 20 MHz and up to 50 kV synchronized to the beam burst by a pickup cylinder. The phase of the deflection is so adjusted that the first portion of the burst to enter the deflecting magnet takes the longest path, and the last to enter takes the shortest path, and the trajectories are arranged to direct and focus the "bunched" beam onto a target of  $\text{D}_2$  or  $\text{T}_2$  gas, where the  $\text{D(d,n)He}^3$  or  $\text{T(d,n)He}^4$  reaction produces a burst of fast neutrons of less than one ns duration. Just before the bunched charged particles strike the target, another pickup cylinder provides a signal which serves to mark the arrival time, which is also the "zero" time for neutron timing (though it is usually delayed to provide an expanded scale of the region of interest in the output of a time-to-pulse-height converter)\*. The Chariot is sketched at the left, and the arrows indicate its direction of motion. On the right, the collimator system is shown in section: the copper shadow cone, the tungsten front collimator, moveable blocks of copper and  $\text{CH}_2$  on a shelf, and the

\* I do not plan to detail electronic "plumbing" either!

main collimator of  $\text{CH}_2$ , with the tungsten-lined throat and additional copper shielding at the front. Arrows indicate the rotation of the collimator system about the scattering sample. Finally, to conclude the "hardware" portion of this presentation, we find in

FIG. 10 a perspective sketch based on photographs of the whole operation. Details not shown in the color slides I used earlier are the "outboard" rear-wheel steering, an overhead guy wire to stiffen the "bowsprit," and the buncher magnet and RF deflection box, which the artist has "stretched" out from their normal position which would have been hidden behind other equipment.

#### MEASUREMENTS OF n-D AND n-T SCATTERING

Since no fast neutron detector exists with either 100% or unequivocally "known" efficiency, "absolute" neutron cross sections must necessarily be either referred to better-known standard cross sections, either point-by-point, or through a chain of calibrations, or else referred to standard flux sources. For time-of-flight measurements, the latter method is not satisfactory, and source reactions are usually intercompared. Scattering measurements are almost universally referred to the  $^1\text{H}(n,n)$  differential cross section, concerning which we have already indicated the present limits of confidence[14,32]. In our series of measurements, neutron flux at each bombarding energy was measured by a separate time-of-flight monitor detector at about  $110^\circ$  to the beam, and the target charge collected was recorded by a stable digital current integrator. The ratio of these numbers was within less than 1 percent from run to run at the same bombarding energy. However, the efficiency of the monitor system was not required to be known, and might be different at different bombarding energies. It was

sufficient that it be stable in time. The product of source flux and detector sensitivity was determined for each incident neutron energy and scattered neutron energy in terms of the properties of the  $^1\text{H}(n,n)$  cross section and the kinematics of elastic scattering. The stability in time could be checked by repeating, at the end of a series of runs at fixed incident energy, a measurement made early in the series, and regular bias-setting checks were made with a  $\text{Cs}^{137}$  source. By making check measurements with differing incident energies so arranged to overlap in scattered energies at the detector, a network of calibrating measurements was developed which gave cross section calibrations directly, and the relative detector efficiency curve as a function of energy indirectly. The scheme of calibration for our measurements is based on the relation

$$E_1/E_0 = 1 - \frac{2 M_1 M_2}{(M_1 + M_2)^2} (1 - \cos\theta'), \quad (1)$$

where  $E_1$  is the scattered energy for incident energy  $E_0$ ,  $M_1$  the scattered mass and  $M_2$  the target mass, and  $\theta'$  the scattered-particle angle in the c.m. system. Using integer particle masses, the numerical factors are

1/2, 4/9, and 3/8 for n-H, n-D, and n-T scattering, respectively.

Thus if one plots  $E_n$  in the laboratory against  $\cos\theta'_{\text{c.m.}}$  for  $E_0 = 9$  MeV, for example, n-H scattering energies will lie on a straight line from 9 MeV at  $\cos\theta' = 1$  to 0 at  $\cos\theta' = -1$ , and n-D scattering energies will lie on a line from 9 MeV at  $\cos\theta' = 1$  to 1 MeV at  $\cos\theta' = -1$ . This is shown in

FIG. 11, together with the pairs of lines for the other three low-energy points at which we took n-D data, 8, 7, and 5.6 MeV, and an additional point at 4 MeV for n-H calibration. Each spot indicates a measurement, circles for n-D and squares for n-H calibrations. The game is to select points such that n-D points are reasonably uniformly spread in  $\cos\theta'$ , but such

that scattered energy points group at a selected smaller set. Now this scheme was subsequently extended to the high-energy group of measurements between 18 and 23 MeV for n-D, and over the whole range for n-T. We thus obtained a tightly-woven mesh of interconnected measurements which imply an efficiency curve, though its actual value is not required, and only its relative slope is needed for second-order corrections due to finite geometry.

Apart from multiple-scattering corrections, this method of calibration in terms of the  ${}^1\text{H}(n,n)$  differential cross section value at the mean scattering angle appears to be valid even with relatively poor angular resolution, as we may show by a simple calculation [33]. The efficiency of detection is proportional to the cross section of  ${}^1\text{H}(n,n)$  scattering at the scattered neutron energy  $E_n$ , which we may approximate as given by

$$\sigma_T = \alpha E_n^{-\frac{1}{2}} - \beta, \quad (2)$$

and we have the other relations

$$E_n = E_0 \cos^2 \theta, \quad (3)$$

$$\sigma_{\text{lab}} = 4 \sigma_{\text{c.m.}} \cos \theta, \text{ and } \sigma_{\text{c.m.}} = \sigma_T/4\pi. \quad (4)$$

We are interested in the cross-section times efficiency product:

$$[\sigma_{\text{lab}}(E_0, \theta) \times \epsilon(E_n)]_{\theta} \sim \sigma_T(E_0) \sigma_T(E_0 \cos^2 \theta) \cos \theta. \quad (5)$$

If we evaluate Eq. (2) in terms of Eq. (3), Eq. (5) becomes

$$[\sigma_{\text{lab}}(E_0) \times \epsilon(E_n)]_{\theta} \sim \sigma_T(E_0) E_0^{-\frac{1}{2}} [1 - \beta \cos \theta E_0^{\frac{1}{2}}], \quad (6)$$

leaving out constant factors. Now if we compare with the average value of the relation (6) integrated over a finite angle from  $\theta - \Delta\theta$  to  $\theta + \Delta\theta$ , and simplify, the ratio may be shown to be

$$R = \frac{[\sigma_{\text{lab}}(E_0)\epsilon(E_n)]_{\theta \pm \Delta\theta}}{[\sigma_{\text{lab}}(E_0)\epsilon(E_n)]_{\theta}} = \frac{1 - \beta E_0^{\frac{1}{2}} \cos\theta (\sin\Delta\theta/\Delta\theta)}{1 - \beta E_0^{\frac{1}{2}} \cos\theta} \quad (7)$$

Evaluated for typical conditions,  $E_0 = 19$  MeV,  $\theta = 58^\circ$ ,  $\Delta\theta = 10^\circ$ , Eq. (7) has the value 1.002. Thus the data calibrated in this manner will differ from the final absolute cross sections only as the incoming attenuation and multiple-scattering factors differ between the hydrogen and deuterium or tritium cases. These corrections will be in the range of 5-10% for our data. We are using a modification of the AWRE "MAGGIE" code for these calculations [34].

Before beginning a review of experimental data, I wish to digress briefly on the use of the Optical Theorem [35], often known as Wick's Limit [36]. This relation states that the c.m. differential cross section for forward scattering of neutrons cannot be less than

$$\sigma_W(0^\circ) = (k\sigma_T/4\pi)^2 \leq \sigma_{e1}(0^\circ), \quad (8)$$

a result which follows from the non-vanishing of the imaginary part of the partial-wave expansion of the scattering amplitude at zero degrees. The result\* is valid for the elastic cross section even with strong non-elastic reaction channels open. The real part of the amplitude will not in general vanish at zero degrees, so Eq. (8) represents a lower limit. As we shall

---

\* Numerically,

$$\sigma_W(0^\circ) = 30.276 E_0 \frac{m_1}{(1 + m_1/m_2)^2} (\sigma_T)^2 \text{ mb/sterad,}$$

for  $E_0$  in MeV and  $\sigma_T$  in barns.

see, for the few-nucleon interactions, it represents a surprisingly good approximation to the extrapolated or fitted cross sections. Physically, the imaginary part of the amplitude is a weighted sum of terms proportional to  $\sin^2 \delta_\ell$ , which is always positive, plus terms which vanish at  $0^\circ$ , and the real part is a similarly weighted sum over terms of the form  $\sin \delta_\ell \cos \delta_\ell$ . When the phases are complex,  $\delta_\ell = \alpha_\ell + i\beta_\ell$ , similar terms occur with the real part  $\alpha_\ell$  substituted for  $\delta_\ell$ , and each term damped by a factor  $e^{-2\beta_\ell}$ . Since the same damping factor occurs in the expression for the total cross section, Eq. (8) still holds, and indeed, may become an even better approximation to the actual  $\sigma_{el}(0^\circ)$ . This would be the case if all significant values of  $\delta_\ell$  were in the same quadrant, so that the sum of terms of the form  $\sin \delta_\ell \cos \delta_\ell$  in the real part has an appreciable value; if we imagine "turning on" damping terms  $e^{-2\beta_\ell}$ , even if the real parts remain  $\alpha_\ell = \delta_\ell$ , the real-part sum would be reduced by the damping action [37]. The case of n-He<sup>3</sup> between 1 and 6 MeV would seem a case in point, as the He<sup>3</sup>(n,p)T cross section is of the order of 1/3 the total cross section, yet  $\sigma_W$  is consistent with least-squares extrapolation of experimental elastic differential cross sections.\* In another extreme example, at low energy one might imagine only one significant s-wave phase shift, in which case

$$\sigma_{el}(0^\circ) = k^{-2} \sin^2 \delta_0, \text{ but} \quad (9)$$

$$\sigma_W(0^\circ) = k^{-2} \sin^4 \delta_0, \quad (10)$$

which is too low by a factor  $\sin^2 \delta_0$  [37]. This is certainly the case for low-energy n-H scattering, where  $\sigma(0^\circ) = \sigma_T/4\pi$ , and  $\sigma_W$  will be an underestimate by the ratio  $\sigma_{el}(0^\circ)/\sigma_W(0^\circ) = 1/k^2 \sigma_{el}(0^\circ)$ . Something of the sort must be

---

\* At 6 MeV, the least-squares extrapolation falls 1.5 standard deviations below  $\sigma_W$ . We will return to this point.

happening in low-energy n-D scattering, though the restriction to  $l = 0$  is hardly valid even at the lowest energy observed, 0.1 MeV. At such an energy, the  $^4S$  phase shift quite dominates the others, and is about  $\sin^{-1}(.25)$ ; this is consistent with the observed values and the underestimate by a factor  $(.25)^2 = 1/16$  suggested by Eq. (9) and (10). A graph of Wick's Limit for the hydrogen isotopes and  $\text{He}^3$  is presented in

FIG. 12, which gives curves for these cases between 0 and 24 MeV, based on measured total cross sections [1,2] (shown in Fig. 1 and Fig. 24 below). Note the very sharp low-energy cutoff for hydrogen, and that the deuterium case is convex upward, while tritium and  $\text{He}^3$  are concave upward at low energy. These values will appear in subsequent differential cross section curves.

#### THE NUCLEON-DEUTERON INTERACTION

Our preliminary data at 5.6 MeV are shown in

FIG. 13, together with several other measurements and calculations. This and all subsequent elastic scattering cross section plots will be of this form, a logarithmic cross section scale and a linear scale in  $\cos\theta'$  c.m.. Wick's Limit is indicated by an arrow at the left. The diamonds are the older n-D data at 5.5 MeV of Wantuck [38], and the triangles are the IASL p-D data of Brolley, Putnam, Rosen, and Stewart at 5.6 [39]. Only a very slight Coulomb interference is seen, before the abrupt rise at small angles. Also shown is the result of calculations by Aaron, Amado, and Yam [40]. These calculations seem to agree in general shape with data between 2.5 and 14 MeV, but are systematically too low in absolute value. Final multiple-scattering and attenuation corrections not yet applied should have relatively little effect, since the H and D total cross sections (cf. Fig. 1) are quite similar. Corrections to

the hydrogen efficiency calibration will result in a reduction in back-angle (low-energy) cross sections due to the greater smearing of the hydrogen spectrum into regions of lower efficiency near the bias cutoff point, but multiple-scattering corrections will bring them back up. I will defer remarking on the  $(n,2n)$  calculations for the moment, and ignore the shaded region on the graph.

FIG. 14 shows our preliminary data at 9 MeV, again as circles, compared with the LASL p-D measurements of Allred, Armstrong, Bondelid, and Rosen [41] at 9.7 MeV, and the calculations for this energy, to which the previous remarks apply. One would expect the p-D data at somewhat higher energy to be a bit too low in cross section for direct comparison, but there is unpublished data from Rice [42] for p-D at 9 MeV which lies just about on the theory curve, so there seems to be a discrepancy in the p-D data. Further unpublished n-D data from Rice [43] at this energy is in reasonable agreement with our preliminary values. There is considerably more data at 14 MeV, as summarized in

FIG. 15. The triangles are the LASL plate camera data of Allred, Armstrong and Rosen [44] which probably suffers from multiple scattering near the minimum; my telescope measurements [4] are shown as circles, and the recent Zagreb data [45] shown as solid diamonds are in good agreement, except perhaps for a systematic difference at back angles where the (recoil) technique is at its best; the 13.9-MeV p-D data of Kikuchi, et al. [46] are shown in open diamonds. The solid curve is a prediction from the analysis of van Oers and Brockman [47,48] based on p-D phase shifts. More recent direct analysis of n-D gives a closely similar curve [22,48]. It has the integral shown, which is consistent with the total cross section and the  $D(n,2n)P$  cross section [27]

in Fig. 1. Wick's Limit is indicated again by an arrow. The calculations of Amado [40] again come out rather too low in absolute value, and those of A. C. Phillips [49] give much too shallow a distribution.

Additional 14-MeV n-D data from UCLA [ 50 ] has just reached me, too late to include in the graph. I have not had time to examine the report in detail, but the principal result is that measurements were carried much farther forward than any of the other data, and show larger values in that region than the curve shown in Fig. 15. A  $C_6D_6$  scintillator time-of-flight technique was employed. The integral of the new data at 14.3 MeV is  $648 \pm 83$  mb which is consistent with the value 616 mb shown for the solid curve in Fig. 15. It implies the non-elastic cross section  $154 \pm 84$  mb at 14.3 MeV (cf Fig. 1).

I showed earlier a survey 3-parameter drawing of the polarization of certain sources [51], and I am about to present another one.

FIG. 16 shows most of the available data on cross sections and polarizations in n-D (shown as solid curves and bars) and p-D (shown as dashed curves and open rectangles) elastic scattering up to 24 MeV. Cross sections are shown on the right, as in the detailed examples just shown, displaced along an oblique energy axis. Starting at the top, here is our preliminary data for n-D at 23, 20.5, 19 and 19.5 combined at 19, and 18 MeV. The only p-D data in this region is that of Caldwell at UCLA [52] at 20.57 MeV which shows a distinct dip of Coulomb interference at forward angles, a phenomenon which becomes more pronounced at 40 [53] and 77 MeV [54]. The situation near 14 MeV we have just discussed [44-50]. At 12.18 [55] and 11.5 MeV [56], the p-D data of van Oers and Brockman are shown, together with van Oers' prediction [48] for n-D based on the p-D phases and suitable higher-order phases calculated in Born Approximation [22,48]. We have already

seen in Figs. 14 and 13 the data at 9 and 5.6 MeV, and the curves shown at 7 and 7.85 are our new n-D data at 7 and 8 MeV, and the p-D data at 7.85 MeV of Brolley et al. at LASL [39]. The remaining curves represent our measurements of n-D at 2.45 and 3.27 MeV [5], as well as those of Brüllmann, Gerber, Meier and Scherrer [57] at 3.27 MeV; work of Elwyn, Lane and Langsdorf [58] at 1.95, 1.0 and 0.5 MeV, and of Allen at 0.2 and 0.1 MeV [20]. The earlier work of Adair, et al. [19] is largely superseded at the energies mentioned, but is in reasonable agreement and provides data at some intermediate points. I am unable to reconcile the sharply-rising forward-angle data of Blanc, et al. [59] for 1.2 and 3.22 MeV with other data or with the general trend of phase shifts [22,48], taken separately. Lower-energy p-D data [60,61] is not too dissimilar to n-D, but has been omitted for clarity. As I warned earlier, each of the distributions has affixed a small arrow at the left corresponding to Wick's Limit. Above 5 MeV, it seems a fairly reliable guide, the p-D distributions tending toward it and then shying off at the last. The n-D curves come in a bit higher, and one of the reasons for this choice of scales is the nearly straight-line trend of the data in the forward hemisphere. The minima move backward with increasing energy, deepening another factor of three between 14 and 23 MeV.

Turning next to the polarizations, we find them displayed on a linear scale, with zero value in the plane, and as data bars rather than as curves. The dashed curves at 2, 10, and 22.7 MeV are theoretical predictions [62] for n-D polarization with tensor forces by Purrington, a student of J. L. Gammel. Since the polarizations are generally small, and the collection rather confusing at best, I have been rather heavy-handed in omitting acceptable but superseded data as well as in ignoring outlying single points. I have retained the mentioned distinction between n-D (solid bars) and p-D (open rectangles), but dropped the distinction between different references at the same or nearby

energies. Included are the p-D results of Trächslin and Brown [63] shown\* at 1.0, 2.1 and 3.1 MeV, n-D data of Behof, et al.[64] and Beghian [65], shown at 1.0, and of Elwyn, et al.[58] at 1.0 and 2.1 MeV; p-D data of Chalmers, et al. at 2.1 MeV; n-D data of Cranberg at 2.1 MeV; p-D data of Shakun, et al. [68], and of Shafroth, et al.[69], at 3.1 and 4.0 MeV, and of Gruebler, Haeberli, and Extermann [70] at 3, 4, 6, 8, and 10 MeV, also of Clegg and Haeberli [71] at 4, 6, 8, 10, and 12 MeV. The n-D measurements of Walter and Kelsey [72] are shown at 2.1, 6, 10, 16.4, and 23.7 MeV. Other low-energy n-D data is that of Brüllman et al.[57] shown at 3.1 MeV, that of Bucker, et al. [73] shown at 3.1 and 4 MeV, and that of Schwarz and Graf [74] shown at 4 MeV. In the high-energy region, we have included p-D results of Rosen and Leland [75] at 14.5 MeV, of Conzett, et al.[76] at 22 MeV, the n-D work at 22.7 MeV of Malanify, Simmons, Perkins, and Walter [77], and the recent p-D work of McKee, et al. [78] at Berkeley for energies of 11, 13.2, 15.7, and 19.1 MeV, which nicely bridge the gaps remaining in the domain pictured. For completeness, the bibliography includes reference to recent p-D polarization measurements at 29 [79], 30.2 [80], 30 and 50 [81], and 40 MeV [82]. A few p-D tensor polarizations have been observed between 4 and 11 MeV [83-85]. I need hardly point out, after that exhausting recitation, that more than half the data points shown or implied have been obtained within the last three years, and that the detail available above 10 MeV is now quite extensive, though clearly more neutron polarization work is desirable. There is surely enough p-D polarization data available to warrant a vigorous theoretical attack on its explication. In passing, it is interesting to note that the development between 14 and 24

---

\*The energies quoted are those at which data has been plotted in Fig. 16, actual measurements may have been within  $\pm 0.5$  MeV of the points quoted.

MeV of a negative portion of the polarization and a rapid return through zero to positive values corresponds rather well with the deepening minima near  $\cos\theta' = -0.5$ , and may be an example of the relation between zeros of polarization and minima in the cross section discussed by Rodberg [86] in terms of the Optical Model, and in somewhat more generality by A. de-Shalit [87,88]. Somewhat similar phenomena appear in the remaining cases I will illustrate shortly, and I would like to see this interesting idea investigated for applicability in the few-nucleon field [89].

#### EMISSION SPECTRA IN PHASE SPACE

As a change of pace from all that data, let us digress for a while and examine the results of a little mathematical exercise. Since the  $(n,2n)$  reactions, at least, are significant in the n-D and n-T interactions, and their presence is a complication in analyzing the elastic scattering data, as their continuous energy spectra will be confused with the "tailing" of the elastic time-spectra due to multiple scattering, we wished to put into the "MAGGIE" calculations a reasonable estimate of their effect. If we assume that the neutrons are emitted isotropically in the c.m. system, and that they are produced in a direct reaction, without sequential decay or final-state interaction, then the energy distribution in the c.m. system for any one of P particles emitted, with equal probability in phase space, will be

$$N(E_i) \sim E_i^{1/2} [E_{i\max} - E_i]^{3/2} P^{-4}, \quad (11)$$

where  $E_{i\max}$  is the maximum energy available to the ith particle, and depends only on the incident energy and Q of the reaction [90,91]. The exponent is 1/2 for  $(n,2n)$  and 3/2 for  $(n,3n)$ . The unfolding to find laboratory spectra is

messy but straightforward, and a program was prepared by R. Lazarus to calculate such spectra, normalized to unity or a specified breakup cross section, and to perform integrations over energy or angle as might be required. A number of such distributions have been included in Leona Stewart's n-T compilation [92].

FIG. 17 illustrates the spectra [93] obtained on this basis from Eq. (11), for  $D(n,2n)P$ . The threshold is 3.35 MeV, and spectra are given for selected laboratory angles and the incident energies between 5 and 23 MeV noted on the curves. Inset in the upper right hand corner is the result of integrating over the spectra to give the angular distributions. The curves are normalized to correspond to the cross sections tabulated, which correspond to Fig. 1. The scales have been multiplied by two to give emission cross sections, where the values tabulated are the absorption or reaction cross sections. This point will come up again when we get to  $He^3$ . Some of these angular distributions were shown on Figs. 13 and 14, but without the factor of two. Since the forward c.m.-to-lab conversion factor is 2.25, those illustrations indicate qualitatively the relative yield of elastic and inelastic neutrons. This is, of course, a calculable idealization. If we compare similar curves for the protons from  $D(n,p)2n$ , in which it is well known that final state interactions are quite pronounced, as seen in

FIG. 18, we note in comparison with the Zagreb data [94] that the prominent peaks are superimposed on a background which, if smeared by the experimental resolution, is in semi-quantitative agreement. Better agreement might be expected for neutron distributions, or for the charge-conjugate reaction  $D(p,2p)n$  proton distribution. Data has been obtained by Kikuchi, et al. [46] at 13.9 MeV, which is indicated by the solid curves in

FIG. 19, compared with the corresponding 3-body breakup spectra, and it is seen that in this case the agreement is best at the forward angles. Thus we have some confidence that this procedure is a reasonable approximation for the purpose intended in our correction calculations. Thus emboldened, we undertook to do the same for  $T(n,2n)D$ , and---just in case it exists after all--- $T(n,3n)P$ .

FIG. 20 gives the results for these cases. The  $(n,2n)$  threshold is 8.35 MeV, and the distributions are a much more rapid function of incident energy than the  $D(n,2n)P$  cases. As before, the inset graph gives angular distributions integrated over the spectra, with a table of the absorption cross sections used for normalization, which correspond to the dashed curve in Fig. 1-guesswork. At the top is an even wilder guess for an assumed small cross section for  $T(n,3n)P$ , which I include primarily to show the effect that the larger exponent in Eq. 11 has on the endpoint, making it unlikely that we could hope to detect it in our data, though well time-resolved. The spectrum shown is for zero degrees. However, if a very strong final-state enhancement occurred near the endpoint, it would be relatively conspicuous. This would correspond to a slowly-moving  $2np$ , or "unglued triton" interaction.

#### THE FOUR-NUCLEON SYSTEMS

Before proceeding into another "bird's-eye" survey of the  $n-T$  and  $p-He^3$  data (which will not be quite so "bristling" with data as was Fig. 16), let us examine the present state of measurements of  $n-T$  scattering near 14 MeV, in

FIG. 21.<sup>\*</sup> Here we may compare LASL data of Leland and Rosen [95] for  $p-He^3$  scattering at 14.5 MeV, shown as solid circles, with three sources of  $n-T$  recoil measurements: the 1951 LASL telescope measurements of Coon, et al. [96] and the recent Zagreb telescope measurements [45], shown as open and closed triangles which seem self-consistent, but quite low---possibly a factor of two at back angles where the technique is best---but not simply by a factor

---

\* This figure was deferred until after the presentation of I. Basar.

independent of angle as might be attributed to an error in assay of the amount of tritium absorbed in metallic foils (a notoriously tricky measurement, incidentally). The situation is not much helped by recent French measurements at CNRS [97], using a "solid recoil-chamber" technique in which the angular distribution in the c.m. system is given directly by the laboratory recoil triton energy distribution in a CsI crystal. Unfortunately, poor statistics and large corrections render the region near the minimum of little value in detail. However, the integral, which weights heavily the least uncertain portions of the distribution, is consistent with the curve shown, which is an estimate of the n-T differential cross section based on the p-He<sup>3</sup> data, the general trend of  $\sigma(0^\circ)/\sigma_W$ , and the measured values of  $\sigma_T$  and  $\sigma_{ne}$ . Basar has informed me that if the Zagreb points are extrapolated to Wick's Limit and integrated, the implied non-elastic cross section is consistent with the value reported [30]. A substantial number of protons and deuterons at small angles have been reported in the Zagreb-Belgrade observations [98]. Perhaps we can yet look forward to finding more evidence for the "unglued triton" as we continue analysis of our high-energy n-T data!

FIG. 22 shows the threatened "birdseye" view of the n-T and p-He<sup>3</sup> data. The bibliography is a bit shorter here. For the cross sections, the n-T results at 1, 2, 3.5, and 6 MeV are from our earlier work [6]; we have repeated the measurement at 6 MeV satisfactorily with the liquid tritium sample, and obtained new complete distributions at 9, 18, 19.5, 21 and 23 MeV. At 1, 2, and 3.5 MeV, the p-He<sup>3</sup> (dashed) curves represent the work of Famularo, et al. [99], and of Tombrello, et al. [100]. The latter work provided distributions to 4.54 MeV, which overlaps later work of Clegg, et al. [101], between 4.5 and 11.5 MeV, and of McDonald, Haerberli, and Morrow [102],

between 4.0 and 12.8 MeV. The sample data selected from this extensive material are the Rice distribution at 7.51 MeV [101], and the Wisconsin data at 10.77 MeV [102].\* The data has been analyzed in terms of phase shifts by Tombrello [103], together with the low-energy data of Kavanagh, et al. [104], and the polarization measurements of the Wisconsin group [102], obtaining a very close representation of the data over this range. The latter polarization data is represented by the fitted curves shown at 9 (actually 8.82) and 10.77 MeV. The only n-T polarization measurements are those we obtained at 1.1 MeV [6], and they are not significantly different from zero, a result that is consistent with the n-T phase shift analysis also made by Tombrello [105], who has provided close fits to our differential cross section data between 1 and 6 MeV, and predicted from his analysis the large polarizations shown for 2, 3.5, and 6 MeV. The most recent contribution to this subject is the unpublished data of the Berkeley group [106,78] extending p-He<sup>3</sup> polarization measurements to 21.3 MeV. The five polarization curves between 21.6 and 11.7 MeV are a representation of this work. Additional data not specifically included at this time will be found in the work of Brolley, et al. at LASL [39], for p-He<sup>3</sup> scattering between 3.5 and 9.7 MeV, of Sweetman [107] at 5 MeV, of Lovberg [108] at 9.75 MeV, of Shakun, et al. [68] between 3.7 and 3.9 MeV, of Drigo, et al. [109] between 2.38 and 4.46 MeV, of Rosen and Brolley [110] at 10 MeV and of Rosen and Leland at 14.5 MeV [75].

---

\*It was the author's intention, and future plan, to first block out the form of Fig. 22 with p-He<sup>3</sup> data most closely comparable with the n-T data, and then to fill in such additional distributions as could be included graphically without reducing clarity. Since the selected curves below 11 MeV are part of sets that have been closely fitted, the ones chosen are representative, but the author regrets that time did not permit fuller representation of the beautifully complete experimental position with respect to p-He<sup>3</sup> scattering and polarization. A more complete realization is in preparation.

Igo and Leland [111] have obtained excitation functions at selected angles in 25-keV steps from 11.6 to 15.6 MeV (and higher unpublished data) in a search for a  $\text{Li}^4$  state near 10.6 MeV. Substantially structureless curves were observed. Similar work between 12.6 and 15.4 MeV has been reported [112]. It has been reported [113] that 5-9 MeV protons scattered by an optically-pumped  $\text{He}^3$  target do not confirm polarizations predicted from Tombrello's phases for polarized proton scattering [102], which are probably not unique. The only p- $\text{He}^3$  cross section data comparable with our 18-23 MeV n-T data is that of Vanetsian and Fedchenko [114] at 19.4 MeV. Even though multiple-scattering corrections are not completed, it appears that the n-T data shows a lower cross section at the minimum than reported for p- $\text{He}^3$ .\* As in the p-D and n-D cases, the minima are deep at the higher energies, and move backward with increasing energy. They are certainly associated with rapidly-changing polarizations, though the latter seem to pass through zero somewhat forward of the minima in these cases. In concluding this section, we see again the close relation between Wick's Limit and the actual forward cross section, particularly at small energies.

#### FAST NEUTRON INTERACTIONS WITH $\text{He}^3$

Though I have no new material of my own to present in this last category, several developments are of interest to collate in the preceding manner. Directly after I presented the work of Perry, et al. at LASL [115,8] on the  $T(p,n)\text{He}^3$  reaction in one of these oblique-energy-axis perspectives, there appeared the work of Wilson, et al. [116] at Wisconsin, and of Goldberg, et al. [117] at LRL extending the field from about 5 to 13 MeV proton energy, but it has taken 6 years to get them all put together on one drawing. The Perry data had also been converted to  $\text{He}^3(n,p)T$  cross sections by the Detailed Balance relation, but only the integrated cross sections were used

---

\* This is also implied by the close agreement between the 19.4 MeV p- $\text{He}^3$  data and the 18-MeV n-T results which will be presented later in this symposium by Debertin.

at the time, and the converted differential cross sections lay dormant. Clearly someone should be prompted to work the whole system out. There were no direct measurements of differential  $\text{He}^3(n,p)\text{T}$  data. What did it was a measurement of the Zagreb group [118] at 14.4 MeV for  $\text{He}^3(n,t)\text{P}$  and  $\text{He}^3(n,p)\text{T}$  (measured from 0 to 180 degrees by detecting both protons and tritons in the forward cone) which revealed a strong similarity to the highest-energy  $\text{T}(p,n)\text{He}^3$  data. The result of this prompting produced

FIG. 23, a representation of all available differential data on this system, a formidable array. The curves for the  $\text{He}^3(n,p)\text{T}$  reaction are all calculated from the  $\text{T}(p,n)\text{He}^3$  cross sections from the Detailed Balance relation discussed below. The only direct measurement is that of the Zagreb group [118] at 14.4 MeV. Its inverse has been calculated in the same manner.

#### DETAILED BALANCE RELATIONS

Assuming invariance with respect to time reversal, the Principle of Detailed Balance states [119] that the complementary reaction cross sections, compared at the same total c.m. energy, are proportional to

$$\left( \frac{\text{density of final states} \times \text{spin degeneracy in final state}}{\text{relative velocity in initial state}} \right) .$$

For two-body reactions, this relation can be put in the form

$$g_1 p_1^2 \sigma_{1 \rightarrow 2} = g_2 p_2^2 \sigma_{2 \rightarrow 1} , \quad (12)$$

where the cross sections are for the indicated directions between states 1 and 2,  $p$  is the momentum, and  $g$  is the product of factors of the form  $(2s + 1)$  for the two particle spins associated with each state. The  $\text{T}(p,n)\text{He}^3$  reaction and its inverse are a particularly simple example, as the spin factors cancel in Eq. (12), and the momentum factors can be manipulated into the form

$$E_n \sigma_{n \rightarrow p} = E_p \sigma_{p \rightarrow n}, \quad (13)$$

where  $E_n$  and  $E_p$  are the corresponding laboratory proton and neutron energies at which the cross sections are to be compared. These differ by the laboratory proton energy at the neutron threshold,  $E_0 = 1.019$  MeV. That is,

$$E_n = E_p - E_0. \quad (14)$$

These relations were used to interconvert the data shown in Fig. 23.

Another case of interest, which should be almost as simple, but can hardly be said to be straightforward, as it has not yet appeared correctly in print, is the  $\text{He}^3(n,d)\text{D}$  reaction. The two identical deuterons give rise to seemingly ineluctable semantic problems. Here the spin-degeneracy factors are 2 for the neutron and  $\text{He}^3$ , and 3 for the deuteron, and if one uses these factors in Eq. (12) and manipulates in terms of laboratory energies  $E_n$  and  $E_d$ , and the threshold  $E_0 = 4|Q|/3 = 4.36$  MeV for the  $\text{He}^3(n,d)\text{D}$  reaction, the ratio of emission cross-sections, which is what the basic definition of cross section gives, may be written

$$\frac{\sigma_{1 \rightarrow 2}}{\sigma_{2 \rightarrow 1}} = \frac{\sigma_{n \rightarrow 2d}}{\sigma_{d \rightarrow n}} = 3(1 - E_0/E_n), \quad (15)$$

$$\text{where } E_d = 3(E_n - E_0)/2. \quad (16)$$

In this case the "State 2" involves two identical deuterons, and if one wants the cross section for the absorption of the neutron by  $\text{He}^3$ , one must divide by two, and obtain

$$\frac{\sigma_{n \rightarrow d}}{\sigma_{d \rightarrow n}} = \frac{3}{2} \left[ 1 - \frac{E_0}{E_n} \right], \quad (17)$$

which is what was used to calculate the absorption cross section shown in Fig. 8 of Ref. 8. Unfortunately, in the proceedings of the London meeting [8], the factor of two showed up inside the bracket, making the first term  $\frac{1}{2}$ .

In preparing a review of n-He<sup>3</sup> cross sections [120], Batchelor and Parker correctly interpreted the misprint, but hastily assumed that (15) was the correct expression, and duly multiplied all the cross sections inferred from D(d,n)He<sup>3</sup> by two. It is only fair to note that they were led into this trap by the paper of Rosen and Brolley [121], which showed beautiful agreement between differential T(p,d)D emission (sic) cross sections at E<sub>0</sub> = 8.34 MeV and a differential curve calculated from D(d,p)T data, for which the stated factor was 1.06. This was nuclear plate work in which both deuterons were detected, i.e., the emission cross section was directly observed. Let us see how this works out. In this case the relation similar to Eq. (17) is given by

$$\frac{\sigma_{p \rightarrow 2d}}{\sigma_{d \rightarrow p}} = 3(1 - E_0/E_p), \quad (18)$$

where E<sub>0</sub> = 5.38 MeV is the corresponding threshold. A relation like Eq. (16) applies for the proton energy. Substituting E<sub>p</sub> = 8.34 MeV in Eq. (18) gives the stated factor 1.06 relating the deuteron emission cross section at E<sub>p</sub> = 8.34 MeV to the D(d,p)T cross section at E<sub>d</sub> = 1.5(8.34 - 5.38) = 4.44 MeV.

FIG. 24 shows the present status of n-He<sup>3</sup> cross section measurements, superseding Fig. 8 of Ref. 8. The total cross sections [1] have not changed, nor have the σ<sub>e1</sub> values, the circles being the integrals of our elastic differential cross sections [6], and the + symbols being from the Columbia [122] recoil-chamber distributions. The He<sup>3</sup>(n,p)T cross section has slithered about somewhat in the interim, favoring the 1965 revision of the ORNL cross sections at low energy [122], now normalized to 1980 mb at 100 keV. The results of the detailed-balance calculations corresponding to Fig. 23 are included at the high-energy end, labelled IRL (1961) [117], and Wisconsin (1961) [116]. The integral of the Zagreb result is also shown. Note that the broad anomaly in the cross section is a distur-

tion of the  $1/v$  extrapolation from thermal energies, but that the high-energy data tend toward a  $1/E$  dependence. The  $\text{He}^3(n,d)\text{D}$  absorption cross section we belabored earlier, is shown with the addition of values calculated from Livermore  $\text{D}(d,n)\text{He}^3$  cross sections [124]. The LASL data previously used is that of Brolley, Putnam and Rosen [125]. It is nice to be able to include the inference from one more  $\text{D}(d,n)\text{He}^3$  datum, that of van Oers and Brockman, which corresponds to  $E_n = 21.2$  MeV. The curve clearly starts down, and I have drawn an extrapolation from that point following a  $1/E$  dependence. The Zagreb result [118] for this reaction (derived from the Legendre terms) is also plotted.

Next, we may examine the charge-conjugate data for  $n\text{-He}^3$  and  $p\text{-T}$  near 14 MeV in

FIG. 25,\* which shows the recent Zagreb telescope data [118] together with unpublished LASL data for  $p\text{-T}$  at 14.6 MeV of Leland and Rosen [127], which is beautifully complete. Note that I have plotted the data corresponding to proton and triton detection with oppositely-oriented triangles, and that these interleave over more than half the solid-angle range. The curve shown is an estimate [37] for  $n\text{-He}^3$  scattering which has an integral consistent with the data shown in Fig. 24, and follows the general trend of relation between neutron and proton charge-conjugate cases, and has a forward cross section only slightly above Wick's Limit, shown again by the ubiquitous arrow. For the final figure, we may examine the  $n\text{-He}^3$  and  $p\text{-T}$  situation in

FIG. 26. For the neutron cross sections, there are our measurements [6] at 1, 2, 3.5, and 6 MeV by time-of-flight, the Columbia recoil distributions [122] at 2.67, 5.0, 8.07, and 17.5 MeV, and the estimate at 14 MeV which we have discussed. The other  $p\text{-T}$  curves are from LASL measurements near 1 and 2 MeV [128], and Minnesota work [129] near 2.67 and 3.5 MeV. LASL data of Brolley, et al. [39] are represented at 6.5 and 8.34 MeV, and the last item is the  $p\text{-T}$  measurement of Vanetsian and Fedchenko [114]. We have reduced the forward cross section at 17.5 MeV to Wick's Limit of 279 mb/sterad from the Columbia extrapolation of  $500 \pm 30$  mb/sterad, which gives an unreasonably large integral [37]. The

---

\* This figure was deferred and included in the presentation of B. Antolković.

broad minimum shown in the recoil-counter data is quite out of line with the general trends for few-nucleon data in this region, and in particular, is not consistent with the p-T data at 14.6 and 19.4 MeV. For once, the polarization situation is more complete for neutrons than for protons, thanks to the recent work of Behof, et al. [130] which provides the n-He<sup>3</sup> data shown at 3.33 and 7.9 MeV. We have reported small polarizations at 1.1 and 2.15 MeV [6], which are also plotted. The p-T data of Shakun, et al. between 2.89 and 3.58 MeV has been condensed at 3.33 MeV, and the remaining item is the LASL measurement of Rosen and Leland [75] at 14.5 MeV, which is strikingly similar to the n-He<sup>3</sup> data at 7.9 MeV.

Note that the forward cross sections at low energy are very closely approximated by the values for Wick's Limit, a point on which we commented when the subject was introduced. Least squares fits to our data extrapolate exactly to Wick's Limit at 1 MeV, are slightly above it at 2 and 3.5 MeV, and actually come 1.5 standard deviations low at 6 MeV. The curve in Fig. 26 has been adjusted to pass through Wick's Limit and still provide a satisfactory representation of the data. A more sophisticated discussion of these matters, and suggestions for experiments with polarized beams and targets, will be found in a recent paper by Drigo, Moschini and Villi at Padova [131]. The development of spin-dependent analogues of the Optical Theorem is also discussed in a paper by R. J. N. Phillips [132]. It appears that closer limits may be calculated from total cross sections measured with initially polarized neutrons.

#### PLANS AND PROSPECTS

We are currently engaged in mechanical changes at the Buncher Facility, to provide a rotating collimator support track more rigid in construction and more flexible in application, including a swiveling collimator support cart riding on the track which can be constrained to point at an off-axis

scattering sample, while the main track pivots under the source, as in polarization measurements which we are about to undertake. As an interim step, a second collimator system similar to that shown in Fig. 10 is under construction, with a smaller pivoting track, as is also a liquid-He<sup>4</sup> cryostat to match the hydrogen-isotope systems. We will shortly undertake studies of n-D and n-He<sup>4</sup> polarizations in the 18-23 MeV range with this equipment, and when backgrounds and artificial assymetries are brought under control, try n-T polarizations which are expected to be large. We are meanwhile considering design and construction of a superconducting spin-precession solenoid. Sampson, at Brookhaven [133], has made a 10-cm thick, 125 kilogauss magnet with conical aperture, and something of this sort would precess by 180° neutrons of up to 27 MeV. For this purpose a uniform field is not required, and it is merely necessary that the line integral along the possible neutron trajectories of interest be reasonably constant, and that the transverse component integral be relatively small. The desired precession is in a screw-sense along the path, and the unwanted precession/<sup>a</sup>tumbling precession. A code is available [134] with which to calculate coil locations and currents in cylindrical symmetry (and with which a conical geometry could be approximated by iteration) from specified field distributions. With it and an accessory line-tracing routine [135], a suitable solenoid should be designable.

We plan in the future to replace the LD<sub>2</sub>-LT<sub>2</sub> cell with a cell for liquid He<sup>3</sup>, and eventually make cross section and polarization measurements with it. We will probably look first at the higher energy neutrons (up to 40 MeV) available with the Tandem and three-stage accelerator combinations. For the latter operation the Vertical accelerator is operated negatively as an up-to-8-MeV ion source for injection into the Tandem, providing charged

particles of up to 24 MeV.

Greater promise of good neutron work in the near future comes from the multi-purpose, high-intensity, klystron-bunched ion source nearing completion by Oak Ridge Technical Enterprises Corporation. This source is also expected this summer, in addition to the polarized source already mentioned [51].

This source features a direct extraction negative-ion duoplasmatron with an off-axis aperture of the type reported by Lawrence, Beauchamp, and McKibben [136]. It will supply direct currents of 50 to 100  $\mu\text{a}$  of  $\text{H}^-$ ,  $\text{D}^-$ , and  $\text{T}^-$  and beam bursts of about  $10^{-9}$  second duration. A few of the many other ions that will also be available are  $\text{O}^-$ ,  $\text{F}^-$ ,  $\text{Br}^-$ , and  $\text{I}^-$ .

The pulsed beam utilizes the two-gap klystron-bunching method to achieve short durations. First the beam is chopped into pulse lengths of 10 to 20 nsec by sweeping the dc beam past a small aperture which is located about 30 cm from the duoplasmatron. This region also contains an einzel lens to focus the ions onto the aperture. The aperture is followed by a gap lens with an acceleration potential of 150 KV. The beam is then deflected  $30^\circ$  onto the accelerator axis by a magnet with a mass times energy product of 18 amu-MeV.

As the beam pulse passes the two gaps of the klystron buncher tube (which is about 50 cm long for protons) the front of the pulse is decelerated and the back of the pulse is accelerated in such a way that at some later time they meet. Less than 1 nsec (fwhm) has been observed on a similar source by C. Moak [137] of Oak Ridge National Laboratory, with a peak pulse height of about 300  $\mu\text{a}$ .

## REFERENCES

1. Los Alamos Physics and Cryogenics Groups, Nucl. Phys. 12, 291 (1959).
2. J. D. Seagrave and R. L. Henkel, Phys. Rev. 98, 666 (1955).
3. J. D. Seagrave, Phys. Rev. 92, 1222 (1953).
4. J. D. Seagrave, Phys. Rev. 97, 757 (1955).
5. J. D. Seagrave and L. Cranberg, Phys. Rev. 105, 1816 (1957).
6. J. D. Seagrave, L. Cranberg, and J. E. Simmons, Phys. Rev. 119, 1981 (1960).
7. L. Cranberg, in Nuclear Forces and the Few-Nucleon Problem, T. C. Griffith and E. A. Power, Editors (Pergamon Press, London, 1960), Vol. II, p. 473.
8. J. D. Seagrave, *ibid*, p. 583.
9. D. J. Hughes and R. B. Schwartz, Neutron Cross Sections, Brookhaven National Laboratory Report BNL-325 (U. S. Government Printing Office, Washington, D. C., 1958), 2nd ed.
10. A. Horsley, AWRE Report AWRE O-23/65, July 1965, and Nucl. Data 2, 243 (1966).
11. J. J. Schmidt, KFK 120, EANDC-E-35 "U" (Feb. 1966).
12. C. E. Engelke, R. E. Benenson, E. Melkonian, and J. M. Lebowitz, Phys. Rev. 129, 324 (1963).
13. J. Lebowitz, WASH-1048 (1964).
14. J. C. Hopkins, "Uncertainties in the Anisotropy of  $^1\text{H}(n,n)$  Scattering," this conference.
15. D. E. Groce and B. D. Sowerby, Nucl. Phys. 83, 199 (1966); D. E. Groce, B. D. Sowerby, and J. M. Morris, Phys. Letters 17, 40 (1965).
16. A. Bratenahl, J. M. Peterson, and J. P. Stoering, Phys. Rev. 110, 921 (1958).

17. J. M. Peterson, A. Bratenahl, and J. P. Stoering, Phys. Rev. 120, 521 (1960).
18. H. B. Willard, J. K. Bair, and C. M. Jones, Phys. Letters 9, 339 (1964).
19. R. K. Adair, A. Okazaki, and M. Walt, Phys. Rev. 89, 1165 (1953).
20. W. D. Allen, A. T. G. Ferguson, and J. Roberts, Proc. Phys. Soc. (London), A68, 650 (1955).
21. D. I. Cooper, D. H. Frisch, and R. L. Zimmerman, from BNL-325, 2nd ed., (unpublished), and Phys. Rev. 90, 339 (1953).
22. J. D. Seagrave and W. T. H. van Oers, "On the n-D Scattering Lengths," this conference; W. T. H. van Oers and J. D. Seagrave, Phys. Letters 24B, 562 (1967).
23. R. A. J. Riddle, A. Langsford, P. H. Bowen, and G. C. Cox, Nucl. Phys. 61, 457 (1965).
24. H. L. Poss, E. O. Salant, G. A. Snow, and L. C. L. Yuan, Phys. Rev. 87, 11 (1952).
25. D. I. Meyer and W. Nyer, Los Alamos Scientific Laboratory Report LA-1279 (1951).
26. L. S. Goodman, Phys. Rev. 88, 686 (1952).
27. H. C. Catron, M. D. Goldberg, R. W. Hill, J. M. LeBlanc, J. P. Stoering, and M. A. Williamson, Phys. Rev. 123, 218 (1961).
28. J. L. Gammel and A. D. Mackellar, Phys. Rev. 133, B1476 (1964).
29. Leona Stewart, private communication.
30. D. S. Mather and L. F. Pain, private communication.
31. J. C. Hopkins, J. T. Martin, and J. D. Seagrave, to be published.
32. J. C. Hopkins, Los Alamos Report LA-DC-8781, 1967.
33. P. W. Keaton, private communication.

34. J. B. Parker, J. W. Towle, D. Sams, W. B. Gilboy, A. D. Purnell, and H. J. Stephens, Nucl. Instr. and Meth. 30, 77 (1964).
35. T. Y. Wu and T. Ohmura, Quantum Theory of Scattering (Prentice-Hall, Inc., New Jersey, 1962), pp. 7, 255-257.
36. G. C. Wick, Phys. Rev. 75, 1459 (1949).
37. Leona Stewart, private discussions and unpublished papers.
38. E. Wantuch, Phys. Rev. 84, 169 (1951).
39. J. E. Brolley, T. M. Putnam, L. Rosen, and L. Stewart, Phys. Rev. 117, 1307 (1960).
40. R. Aaron, R. D. Amado, and Y. Y. Yam, Phys. Rev. 140, B1291 (1965).
41. J. C. Allred, A. H. Armstrong, R. O. Bondelid, and L. Rosen, Phys. Rev. 88, 433 (1952).
42. W. D. Simpson, Thesis, Rice University (1965).
43. B. E. Bonner, Thesis, Rice University (1965).
44. J. C. Allred, A. H. Armstrong, and L. Rosen, Phys. Rev. 91, 90 (1953).
45. P. Tomáš, private communication. See the paper presented by I. Basar, this symposium.
46. S. Kikuchi, J. Sanada, S. Suwa, I. Hayashi, K. Nisimura, and K. Fukunaga, J. Phys. Soc. Japan 15, 749 (1960).
47. W. T. H. van Oers and K. W. Brockman, Nucl. Phys. A92, 561 (1967).
48. W. T. H. van Oers, private communication.
49. A. C. Phillips, Phys. Rev. 142, 984 (1966).
50. A. Berick, Thesis, UCLA (1967).
51. J. D. Seagrave, "Sources of Polarized Neutrons," this conference.
52. D. O. Caldwell and J. R. Richardson, Phys. Rev. 98, 28 (1955).
53. J. H. Williams and M. K. Brussel, Phys. Rev. 110, 136 (1958).
54. M. Davison, H. W. K. Hopkins, L. Lyons, and D. F. Shaw, Nucl. Phys. 45, 423 (1963).
55. W. T. H. van Oers and K. W. Brockman, Nucl. Phys. 27, 189 (1960).

56. K. W. Brockman and W. T. H. van Oers, in Nuclear Forces and the Few Nucleon Problem, T. C. Griffith and E. A. Power, Editors (Pergamon Press, London, 1960) Vol. I, p. 481.
57. M. Brüllmann, H. J. Gerber, D. Meier, and P. Scherrer, *Helv. Phys. Acta* 32, 511 (1959).
58. A. J. Elwyn, R. O. Lane, and A. Langsdorf, *Phys. Rev.* 128, 779 (1962).
59. G. Vedrenne, D. Blanc, and F. Cambou, *J. Phys.* 24, 801 (1963).
60. R. Sherr, J. M. Blair, H. R. Kratz, C. I. Bailey, and R. F. Taschek, *Phys. Rev.* 72, 662 (1947).
61. R. J. S. Brown, G. D. Freier, H. D. Holmgren, W. R. Stratton, and J. L. Yarnell, *Phys. Rev.* 88, 253 (1952).
62. R. D. Purrington, Thesis, Texas A. and M. University (1966).
63. W. Trächslin and L. Brown, *Nucl. Phys.* 90, 593 (1967).
64. A. F. Behof, G. P. Lietz, S. F. Trevino, and S. E. Darden, *Nucl. Phys.* 45, 253 (1963).
65. I. E. Beghian, K. Sugimoto, M. Wachter, and J. Weber, *Nucl. Phys.* 42, 1 (1963).
66. R. A. Chalmers, R. S. Cox, K. K. Seth, and E. N. Strait, *Nucl. Phys.* 62, 497 (1965).
67. L. Cranberg, *Phys. Rev.* 114, 174 (1959).
68. N. A. Shakun, A. G. Strashinskii, and A. P. Klyucharev, *JETP* 46, 167 (1964); *JETP (transl.)* 19, 120 (1964).
69. S. M. Shafroth, R. A. Chalmers, E. N. Strait, and R. E. Segel, *Phys. Rev.* 118, 1054 (1960).
70. W. Gruebler, W. Haeberli, and P. Extermann, *Nucl. Phys.* 77, 394 (1966).
71. T. B. Clegg and W. Haeberli, *Nucl. Phys.* A95, 608 (1967).
72. R. L. Walter and C. A. Kelsey, *Nucl. Phys.* 46, 66 (1963).

73. W. P. Bucher, W. B. Beverly, G. C. Cobb, and F. L. Hereford, Nucl. Phys. 13, 164 (1959).
74. E. Schwarz and E. Graf, Helv. Phys. Acta 37, 223 (1964); 38, 877 (1965).
75. L. Rosen and W. T. Leland, Phys. Rev. Letters 8, 379 (1962).
76. H. E. Conzett, G. Igo, and W. J. Knox, Phys. Rev. Letters 12, 222 (1964).
77. J. J. Malanify, J. E. Simmons, R. B. Perkins, and R. L. Walter, Phys. Rev. 146, 632 (1966).
78. J. S. C. McKee, D. J. Clark, R. J. Slobodrian, and W. F. Tivol, Phys. Letters 24B, 240 (1967) and private communication.
79. S. J. Hall, A. R. Johnston, and R. J. Griffeths, Phys. Letters 14, 212 (1965).
80. A. R. Johnston, W. R. Gibson, J. H. P. C. Megaw, R. J. Griffeths, and R. M. Eisberg, Phys. Letters 19, 289 (1965).
81. S. J. Hall, W. R. Gibson, A. R. Johnston, R. J. Griffeths, E. A. McClatchie, K. M. Knight, Comptes Rendus du Congrès International de physique nucléaire Paris, 1964, p. 219.
82. H. S. Goldberg, UCRL-11526, August 1964.
83. P. G. Young, M. Ivanovich, and G. G. Ohlsen, Phys. Rev. Letters 14, 831 (1965).
84. J. Arvieux, R. Beurtey, J. Goudergues, M. Lechaczinski, B. Mayer, T. Mikumo, A. Papineau, and J. Thirion, in Proc. 2nd Int. Symposium on Polarization Phenomena of Nucleons, P. Huber and H. Schopper, Eds., Birkhauser Verlag (1966), p. 370.
85. H. B. Willard, S. T. Thornton, and C. M. Jones, *ibid*, p. 374.
86. L. S. Rodberg, Nucl. Phys. 15, 72 (1959).
87. A. de-Shalit, in "Preludes in Theoretical Physics", A. de-Shalit, *et al.*, eds. North Holland (1966), p. 35.
88. J. Hüfner and A. de-Shalit, Phys. Letters 15, 52 (1965).
89. J. S. C. McKee, private communication.

90. A. D. Fokker, H. D. Kloosterman, and F. J. Belinfante, *Physica* 1, 705 (1933-34).
91. E. Fermi, Elementary Particles (Yale Univ. Press, New Haven, Connecticut, 1951), p. 44.
92. L. Stewart, Los Alamos Scientific Laboratory Report LA-3270 (1965).
93. R. Lazarus, private communication.
94. K. Ilakovac, L. G. Kuo, M. Petravić, I. Šlaus, and P. Tomaš, *Phys. Rev. Letters* 6, 356 (1961); *Nucl. Phys.* 43, 254 (1963).
95. W. T. Leland and L. Rosen, WASH-1064 (1965)(unpublished).
96. J. H. Coon, C. K. Bockelman, and H. H. Barschall, *Phys. Rev.* 81, 33 (1951).
97. D. Blanc, F. Cambou, M. Niel and G. Vedrenne, *J. de Phys.*, Colloq. No. 1 (1966), C1-98.
98. V. Ajdačić, M. Cerineo, B. Lalović, G. Pačić, I. Šlaus, and P. Tomaš, *Phys. Rev. Lett.* 14, 442 and 444 (1965).
99. K. F. Famularo, R. J. S. Brown, H. D. Holmgren, and T. F. Stratton, *Phys. Rev.* 93, 928 (1954).
100. T. A. Tombrello, C. Miller Jones, G. C. Phillips, and J. L. Weil, *Nucl. Phys.* 39, 541 (1962).
101. T. B. Clegg, A. C. O. Barnard, J. B. Swint, and J. L. Weil, *Nucl. Phys.* 50, 621 (1964).
102. D. G. McDonald, W. Haeblerli, and L. W. Morrow, *Phys. Rev.* 133, B1178 (1964).
103. T. A. Tombrello, *Phys. Rev.* 138, B40 (1965).
104. R. W. Kavanagh and P. D. Parker, *Phys. Rev.* 143, 779 (1966).
105. T. A. Tombrello, *Phys. Rev.* 143, 772 (1966).

106. W. F. Tivol, D. J. Clark, H. E. Conzett, J. S. C. McKee, E. Shield, and R. J. Slobodrian, *Bull. Am. Phys. Soc.* 11, 896 (1966), and W. F. Tivol, Private Communication. The author is indebted to Dr. Tivol for preliminary results in advance of publication, and for permission to represent them by the curves shown in Fig. 22.
107. D. Sweetman, *Phil. Mag.* 46, 358 (1955).
108. R. H. Lovberg, *Phys. Rev.* 103, 1393 (1956).
109. L. Drigo, C. Manduchi, G. C. Nardelli, M. T. Russo-Manduchi, G. Tornielli, and G. Zannoni, *Nucl. Phys.* 89, 632 (1966).
110. L. Rosen and J. E. Brolley, *J. de Physique* 21, 365 (1960).
111. G. J. Igo and W. T. Leland, *Phys. Rev.* 154, 950 (1967).
112. P. F. Donovan, J. V. Kane, J. F. Mollenauer, D. Boyd, P. D. Parker, and Č. Zupančič, *Bull. Am. Phys. Soc.* 11, 9 (1966); *Phys. Rev.* 158, 973 (1967).
113. D. H. McSherry, S. D. Baker, D. O. Findley, and G. C. Phillips, *Bull. Am. Phys. Soc.* 12, 86 and 189 (1967).
114. R. A. Vanetsian and E. D. Fedchenko, (transl.) *Sov. Jour. Atom. Energ.* 2, 141 (1957).
115. J. E. Perry, E. Haddad, R. L. Henkel, G. A. Jarvis, and R. K. Smith (unpublished), and Ref. 8.
116. W. E. Wilson, R. L. Walter, and D. B. Fussan, *Nucl. Phys.* 27, 421 (1961).
117. M. D. Goldberg, J. D. Anderson, J. P. Stoering, and C. Wong, *Phys. Rev.* 122, 1510 (1961).
118. B. Antolković, G. Paić, P. Tomaš, and D. Rendić, *Phys. Rev.* 159, 777 (1967). and F. Tomaš, Private Communication. These results will be presented by B. Antolković in a paper at this symposium.
119. W. S. C. Williams, *An Introduction to Elementary Particles*, Academic Press, London (1961), p. 92.
120. R. Batchelor and K. Parker, AWRE Report No. 0-78/64 (1964).
121. L. Rosen and J. E. Brolley, *Phys. Rev. Lett.* 2, 98 (1959).
122. A. R. Sayres, K. W. Jones and C. S. Wu, *Phys. Rev.* 122, 1853 (1961).
123. R. L. Macklin and J. H. Gibbons, EANDC Conference on Study of Nuclear Structure with Neutrons, Antwerp, 1965, P/13.

- M. D. Goldberg and J. M. LeBlanc, Phys. Rev. 119, 1992 (1960).
- J. E. Brolley, T. M. Putnam, and L. Rosen, Phys. Rev. 107, 821 (1957).
126. W. T. H. van Oers and K. W. Brockman, Jr., Nucl. Phys. 48, 625 (1963).
127. W. T. Leland and L. Rosen, Private Communication. The author appreciates permission to present this data in this form, prior to publication.
128. M. E. Ennis and A. Hemmendinger, Phys. Rev. 95, 772 (1954).
129. R. S. Claassen, R. J. S. Brown, G. D. Freier, and W. R. Stratton, Phys. Rev. 82, 589 (1951).
130. A. F. Behof, J. M. Hevezi, and G. Spalek, Nucl. Phys. 84, 290 (1966).
131. L. Drigo, G. Moschini and C. Villi, INFN/BE-67/1 (Preprint communicated by Prof. Villi).
132. R. J. N. Phillips, Nucl. Phys. 43, 413 (1963).
133. W. B. Sampson, BNL-9490 (1965).
134. R. F. Holsinger, UCRL-16958 (unpublished) (1967).
135. M. W. Garrett, ORNL-3575 (1965).
136. G. P. Lawrence, R. K. Beauchamp, and J. L. McKibben, Nucl. Instr. and Meth. 32, 357 (1965).
137. C. Moak, Private Communication to P. W. Keaton.

## FIGURE LEGENDS

- FIG. 1 Total and non-elastic fast-neutron cross sections for the three isotopes of hydrogen, given as a function of neutron energy on a log-log scale between 0.1 and 30 MeV. References are given in text.
- FIG. 2 Transition temperatures for the three isotopes of hydrogen, in degrees Kelvin. Pressures are given in mm of Hg (Torr).
- FIG. 3 Cross section of a cryostat designed to hold one mole of liquid tritium in a thin-walled cell as a neutron scattering sample.
- FIG. 4 Caricature of the gas-handling "chariot" designed to provide neutron scattering samples of the three liquid hydrogen isotopes.
- FIG. 5 Absorption coefficients for neutron shielding by W, Cu, Fe, Pb, and  $B^{10}$  calculated using non-elastic cross sections, and for H in the density of polyethylene ( $CH_2$ ), using the total cross section.
- FIG. 6 Schematic plan view of the use of a "shadow bar" in fast-neutron collimation. Limit lines are discussed in the text.
- FIG. 7 Sketch of shadow bar in use with automatic positioning system. Lines A and B correspond to the lines A and B in Fig. 6.
- FIG. 8 Rectangular-aperture fast-neutron collimator with adjustable throat angles. Shape and assembly of parts 1 through 5 is described in the text.
- FIG. 9 Plan view of the LASL time-of-flight apparatus as used for the n-D and n-T scattering experiments, showing relation of the cryostats and gas-handling Chariot, the beam Buncher, and the neutron-detector collimation system which pivots about the scattering-sample position.

- FIG. 10 Sketch of the LASL time-of-flight apparatus in use, based on a photograph.
- FIG. 11 Graph of the linear relation between scattered-neutron laboratory energy (left-hand vertical scale) and the cosine of the center-of-mass scattering angle  $\theta'$ . Squares and broken lines are for n-P scattering; circles and solid lines are for n-D scattering. Cases shown are for incident energies of 4, 5.6, 7, 8, and 9 MeV. Fifty-four measurements are indicated, at only 12 energies of detector calibration in terms of n-P scattering. Curves give  $\theta_{lab}$  (r.h. scale).
- FIG. 12 Minimum cross section for forward scattering of fast neutrons by hydrogen (H), deuterium (D), tritium (T), and  $He^3$  as a function of neutron energy, based on the total cross sections shown in Figs. 1 and 23. The relation given by the Optical Theorem, also known as Wick's Limit, is written in the upper right-hand corner of the graph.
- FIG. 13 Preliminary LASL data for n-D elastic scattering at 5.6 MeV, compared with other data and calculations identified in text.
- FIG. 14 Preliminary LASL data for n-D elastic scattering at 9 MeV, compared with other data and calculations identified in text.
- FIG. 15 Differential cross sections for n-D and p-D elastic scattering near 14 MeV.
- FIG. 16 Graphical review of n-D and p-D elastic scattering and cross-section polarization data presented as families of graphs displaced along an oblique energy axis. Solid curves and bars represent n-D data, dashed cross section curves and open rectangles represent p-D data. References are given in text. Cross section scale is logarithmic. Arrows indicate values for Wick's Limit (see Fig. 12).

- FIG. 17 Neutron spectra expected from phase-space considerations for  $D(n,2n)P$  breakup for selected incident energies and laboratory angles. Angular distributions in the laboratory system, integrated over the spectra, are given in the inset graph, together with the values of the non-elastic cross section used for normalization (from Fig. 1). Scales have been multiplied by two to give neutron emission values.
- FIG. 18 Comparison of phase-space calculation of  $D(n,p)2n$  proton distributions with Zagreb data at 14 MeV.
- FIG. 19 Comparison of phase-space calculation of  $D(p,2p)N$  proton distributions with the data of Kikuchi at 13.9 MeV.
- FIG. 20 Neutron spectra expected from phase-space considerations for  $T(n,2n)D$  and  $T(n,3n)P$  breakup for selected incident energies and laboratory angles. Angular distributions in the laboratory system integrated over the spectra are given in the inset graph, together with the values of the non-elastic cross section used for normalization (from Fig. 1). Scales have been multiplied by the number of neutrons emitted per reaction to give neutron emission values.
- FIG. 21 Differential cross sections for  $n-T$  and  $p-He^3$  elastic scattering near 14 MeV.
- FIG. 22 Graphical review of  $n-T$  and  $p-He^3$  elastic scattering cross section and polarization data presented as families of graphs displaced along an oblique energy axis. Solid curves and bars represent  $n-T$  data, dashed curves and open rectangles represent  $p-He^3$  data. References are given in text. Arrows indicate values for Wick's Limit (see Fig. 12). Cross section scale is logarithmic.

- FIG. 23 Differential cross sections for the  $T(p,n)He^3$  reaction and corresponding values for  $He^3(n,p)T$  calculated by Detailed Balance, displaced along oblique energy axes. The cross section scales are linear. Recent Zagreb data on  $He^3(n,t)P$  has been presented as  $He^3(n,p)T$ , and converted over to  $T(p,n)He^3$ . Note that the algebraic sense of  $\cos\theta'$  variation is opposite for the two families of curves.
- FIG. 24 Cross sections for the interaction of fast neutrons with  $He^3$ , given as a function of energy on a log-log scale between 0.01 and 30 MeV. References are given in text.
- FIG. 25 Differential cross sections for  $n-He^3$  and  $p-T$  elastic scattering near 14 MeV.
- FIG. 26 Graphical review of  $n-He^3$  and  $p-T$  elastic scattering cross section and polarization data presented as families of graphs displaced along an oblique energy axis. Solid curves and bars represent  $n-He^3$  data, dashed curves and open rectangles represent  $p-T$  data. References are given in text. Arrows indicate values for Wick's Limit (see Fig. 12). Cross section scale is logarithmic.

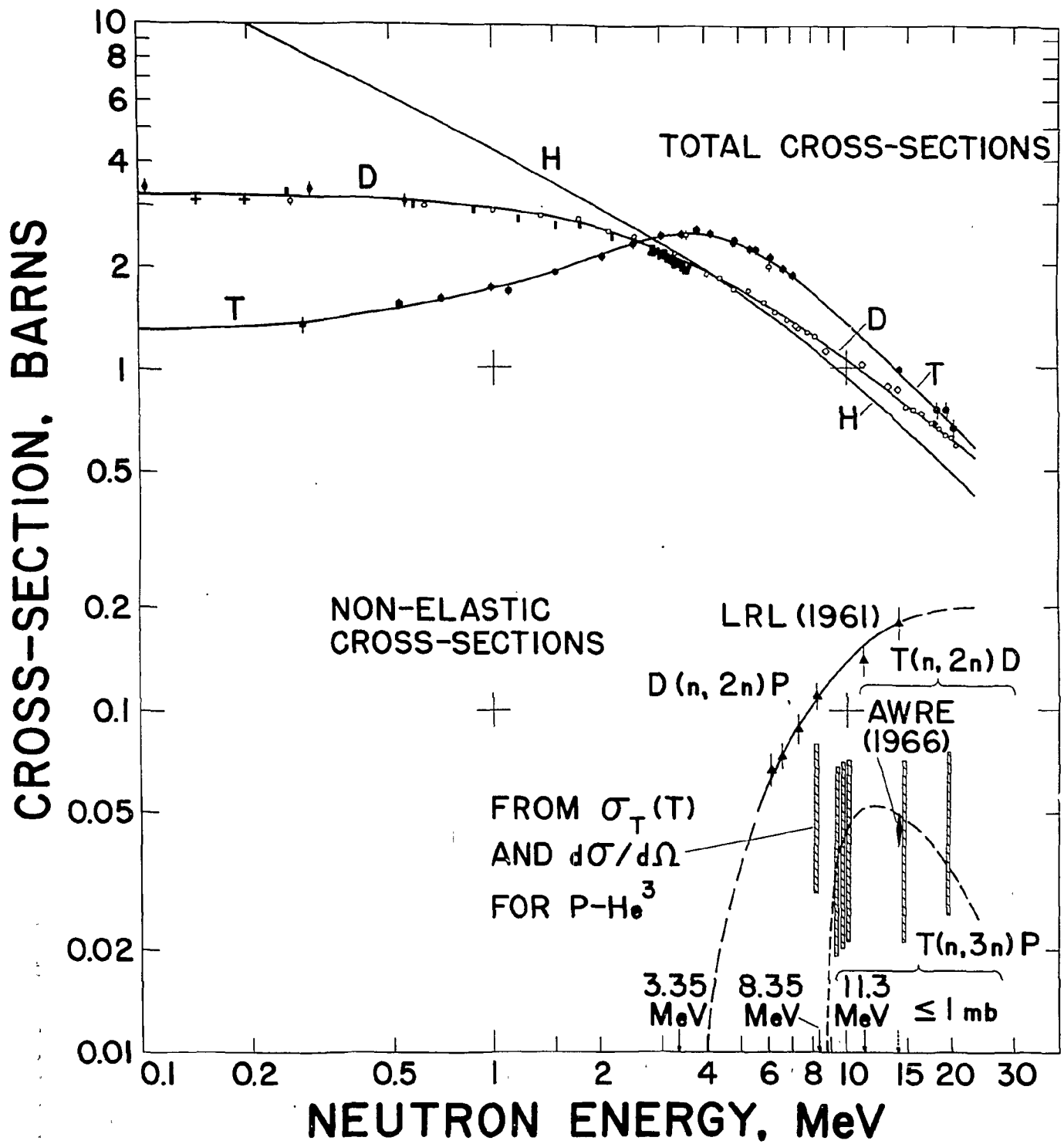


FIG. 1

# TRANSITION TEMPERATURES of HYDROGEN ISOTOPES

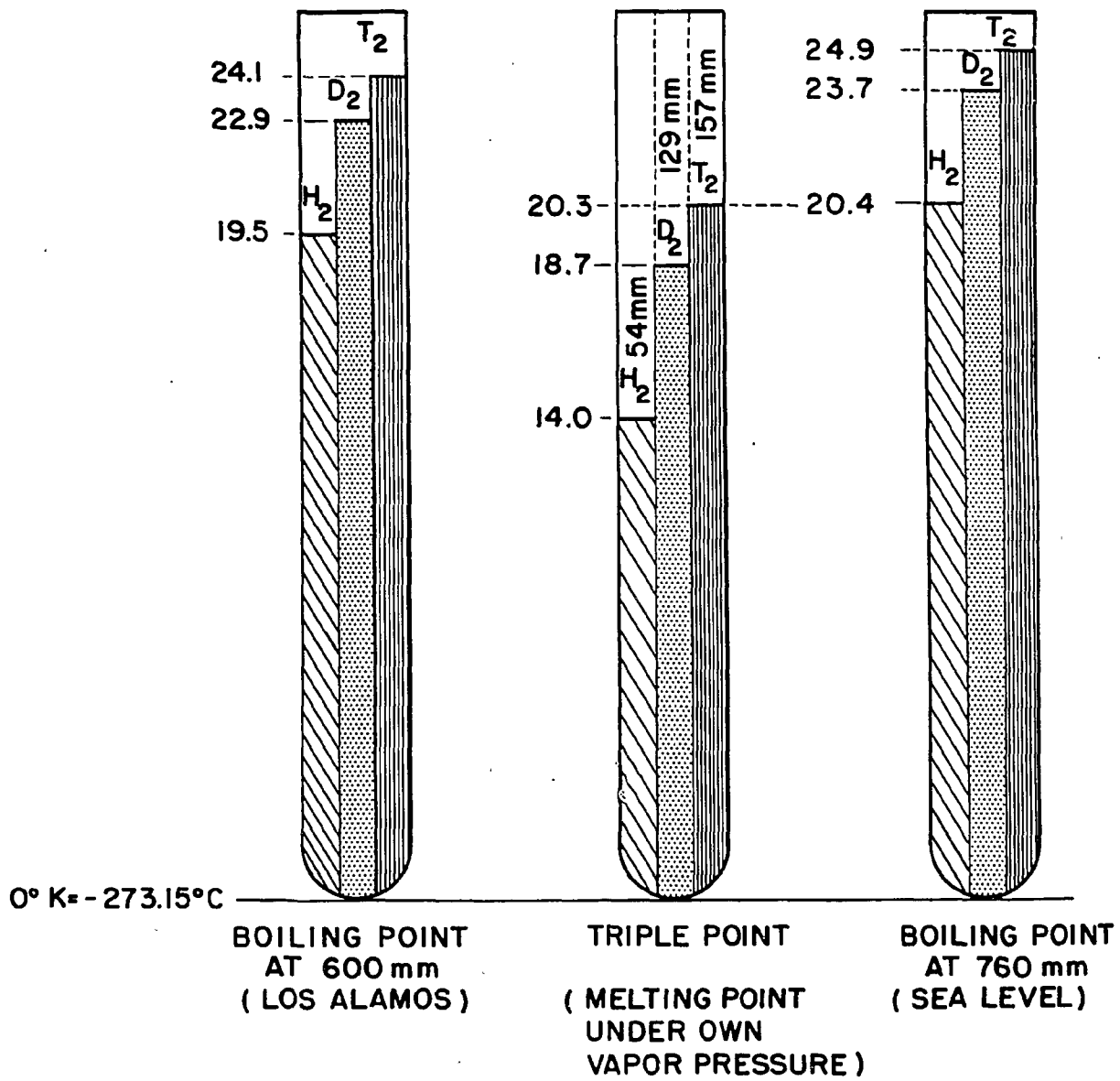


FIG. 2

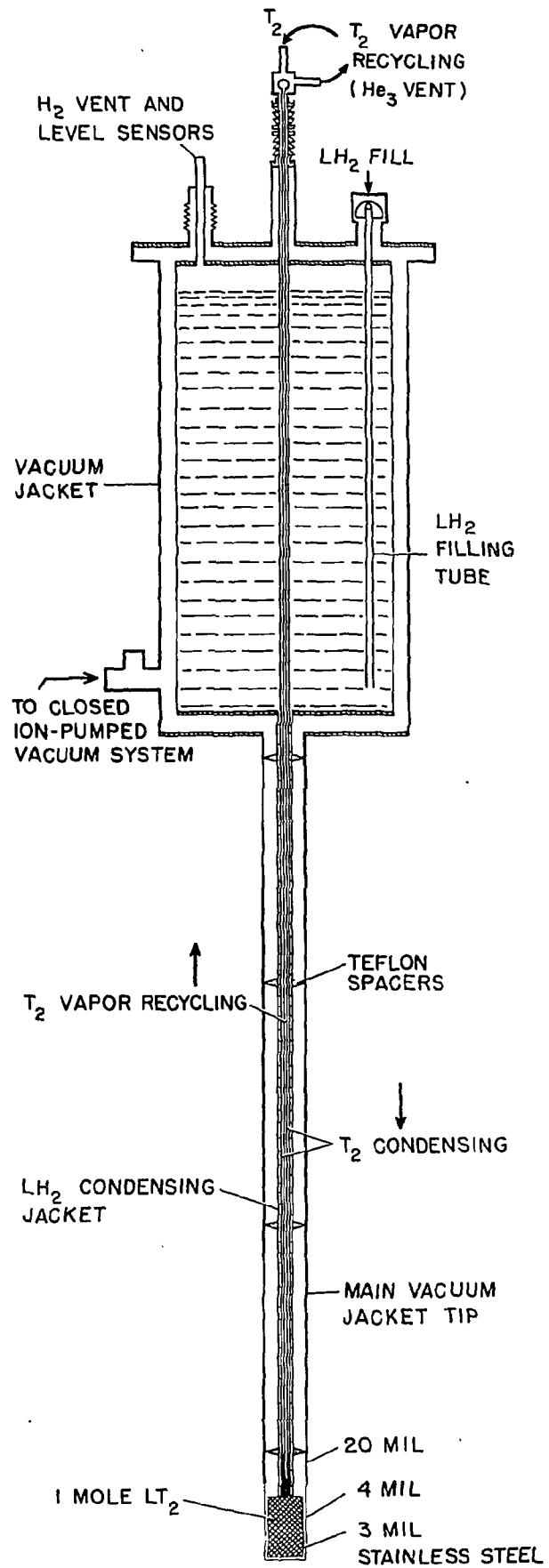
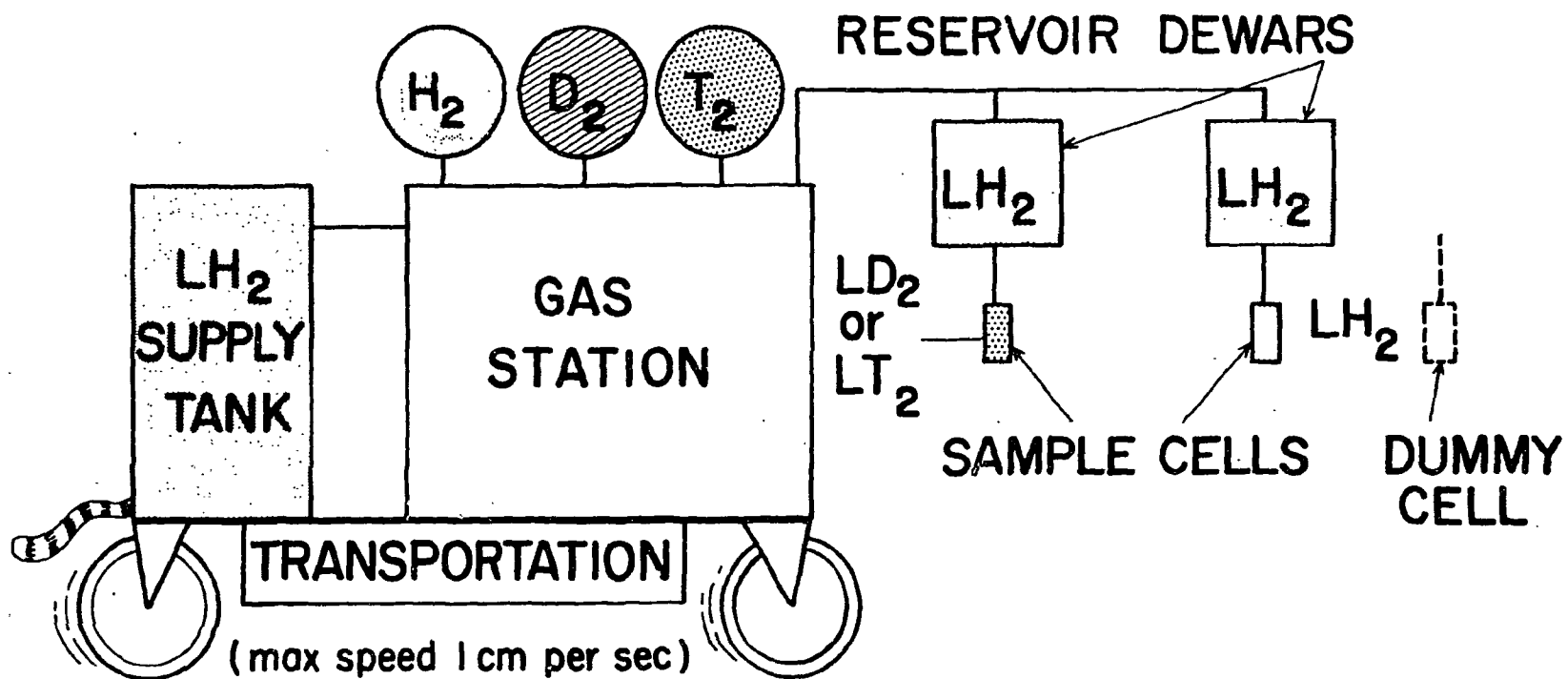


FIG. 3



**MOBILE LIQUID-HYDROGEN-ISOTOPE SCATTERING  
 SAMPLE SUPPLY SYSTEM**

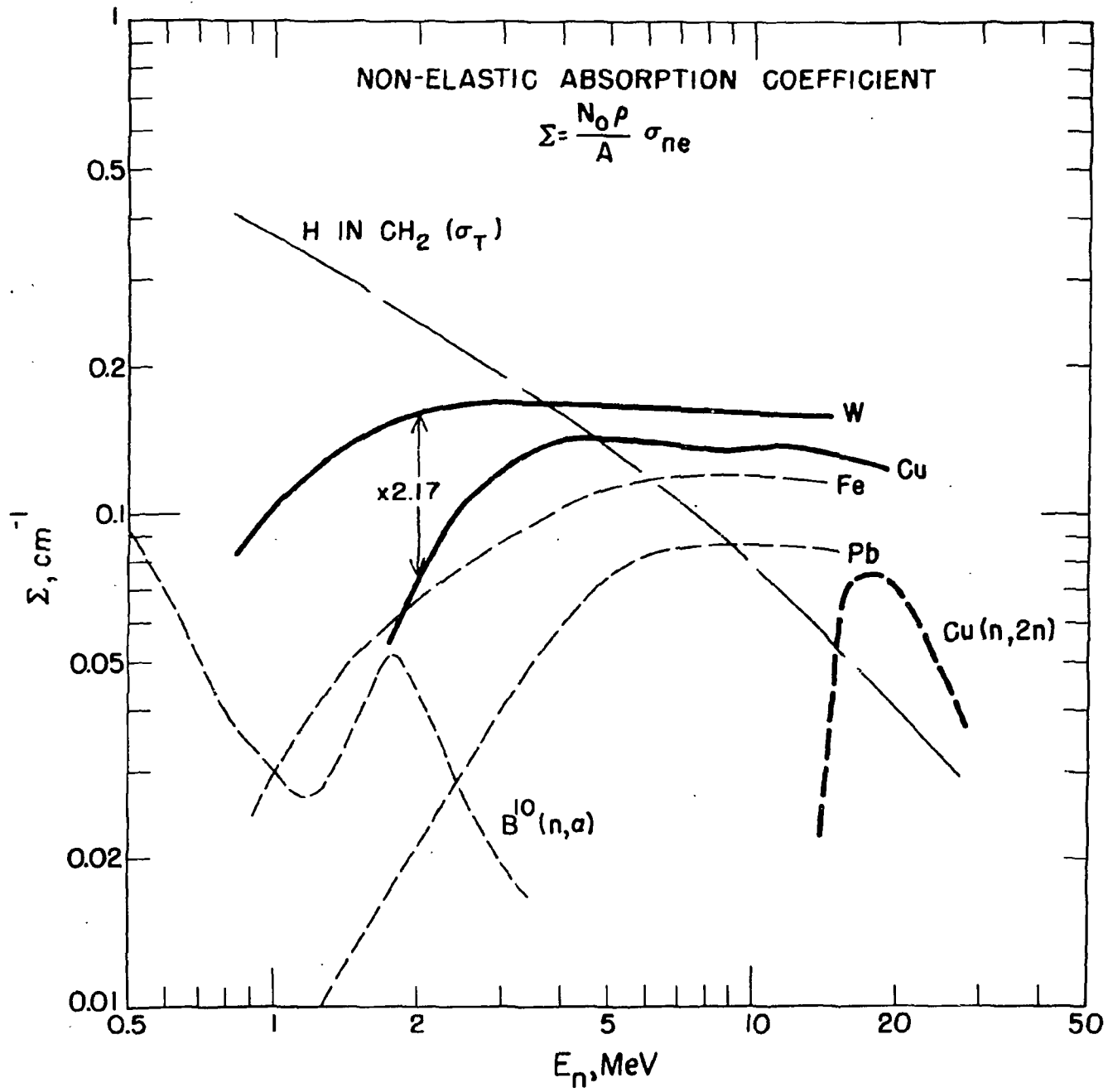


FIG. 5

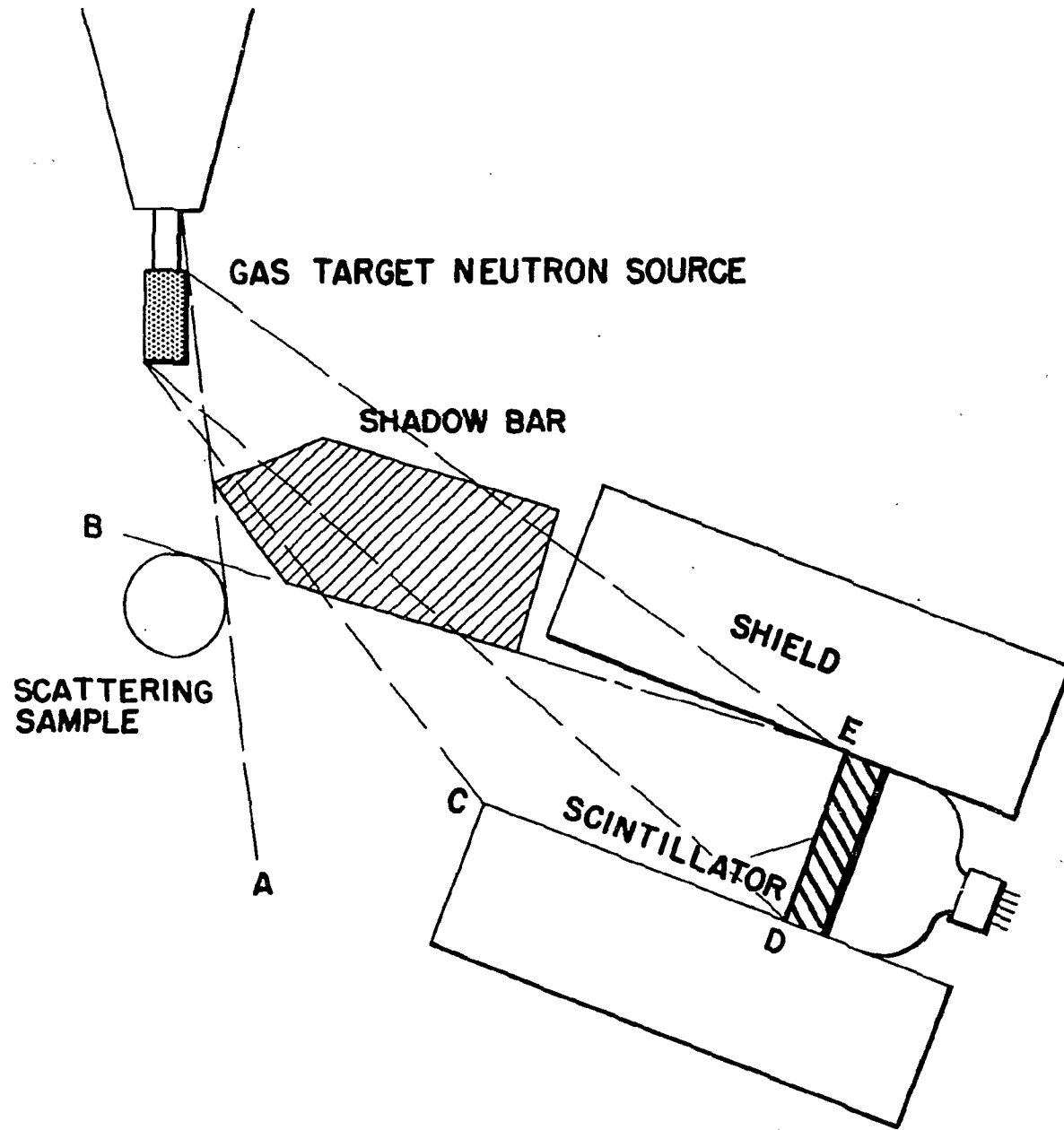


FIG. 6

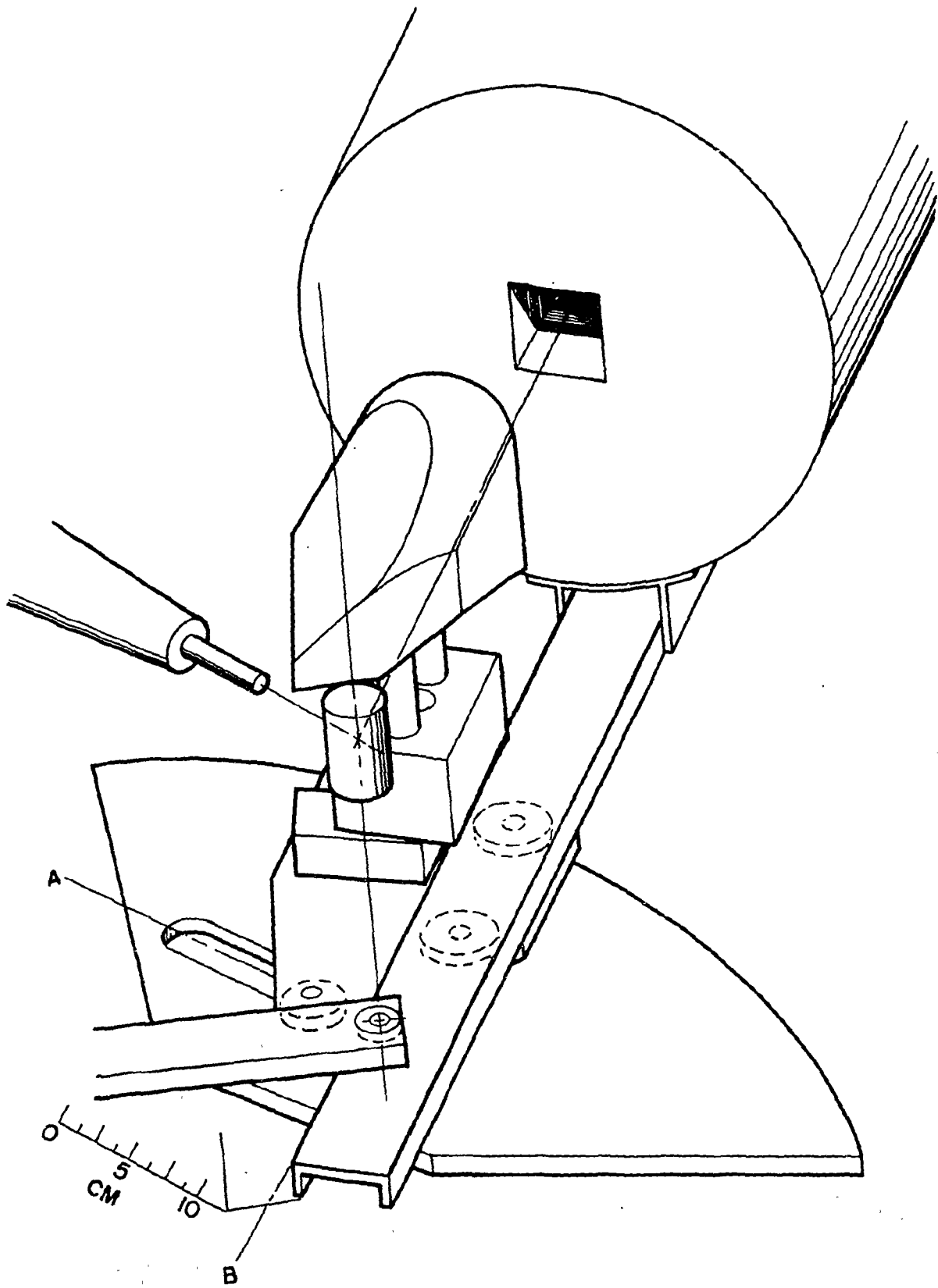
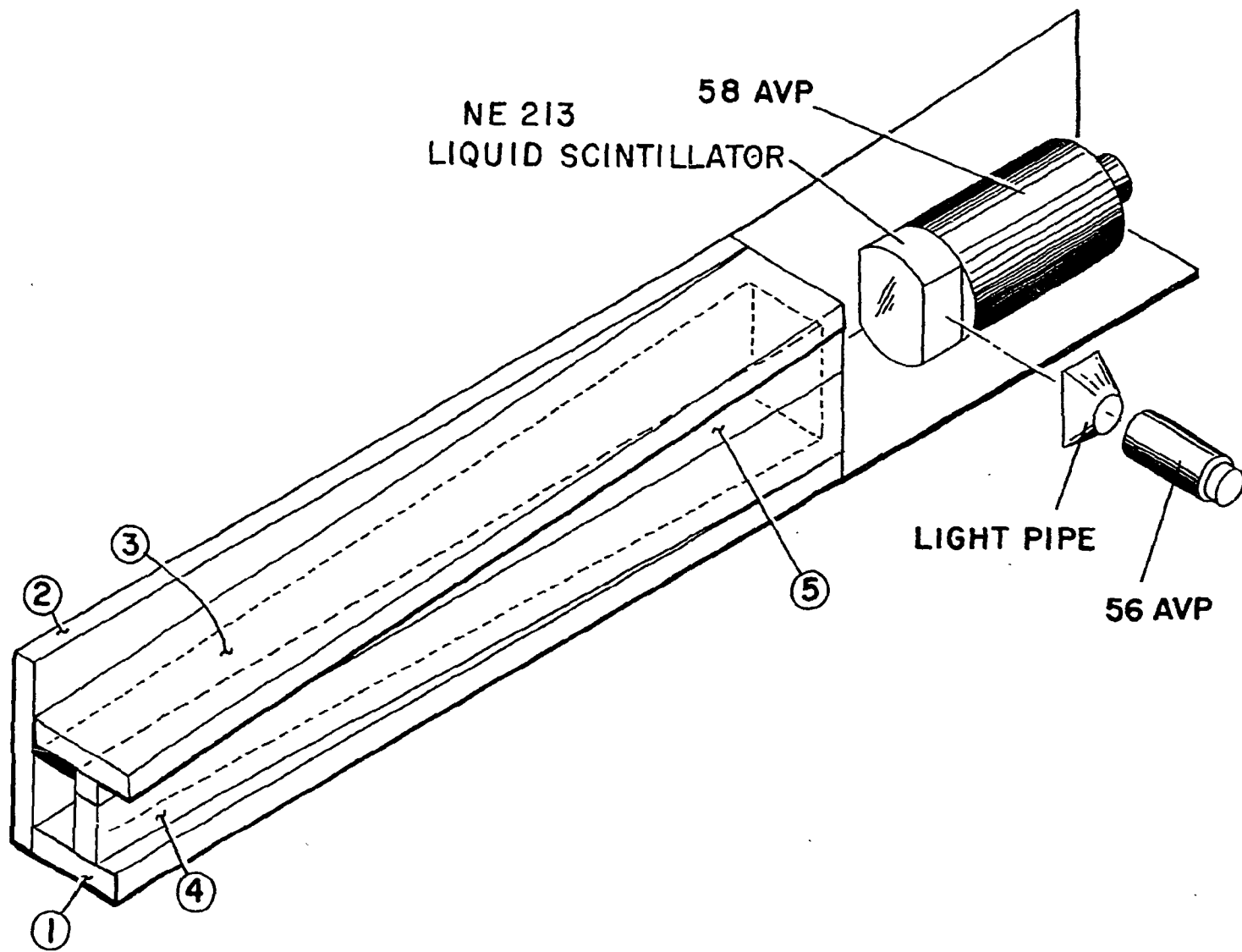
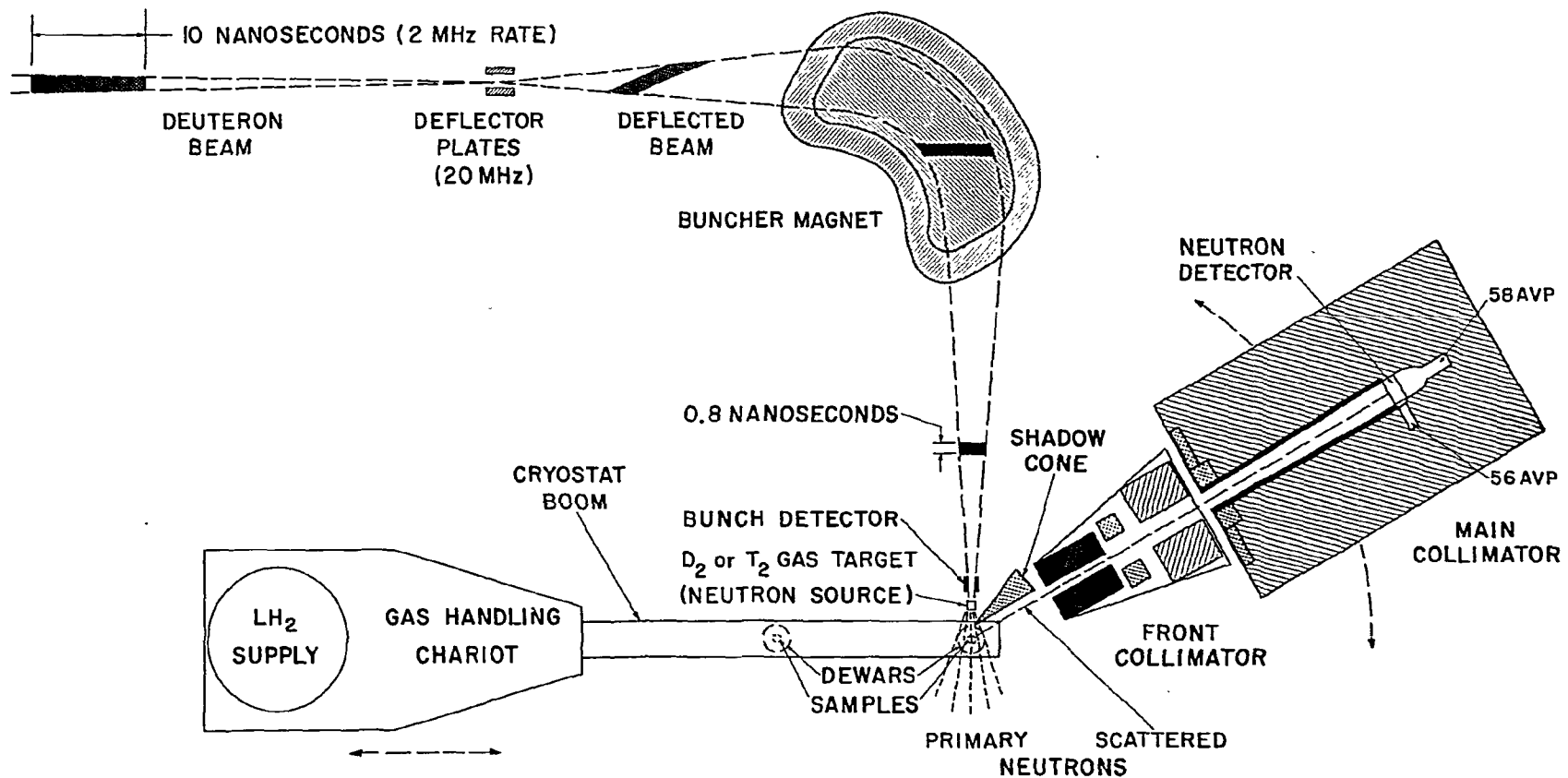


FIG. 7

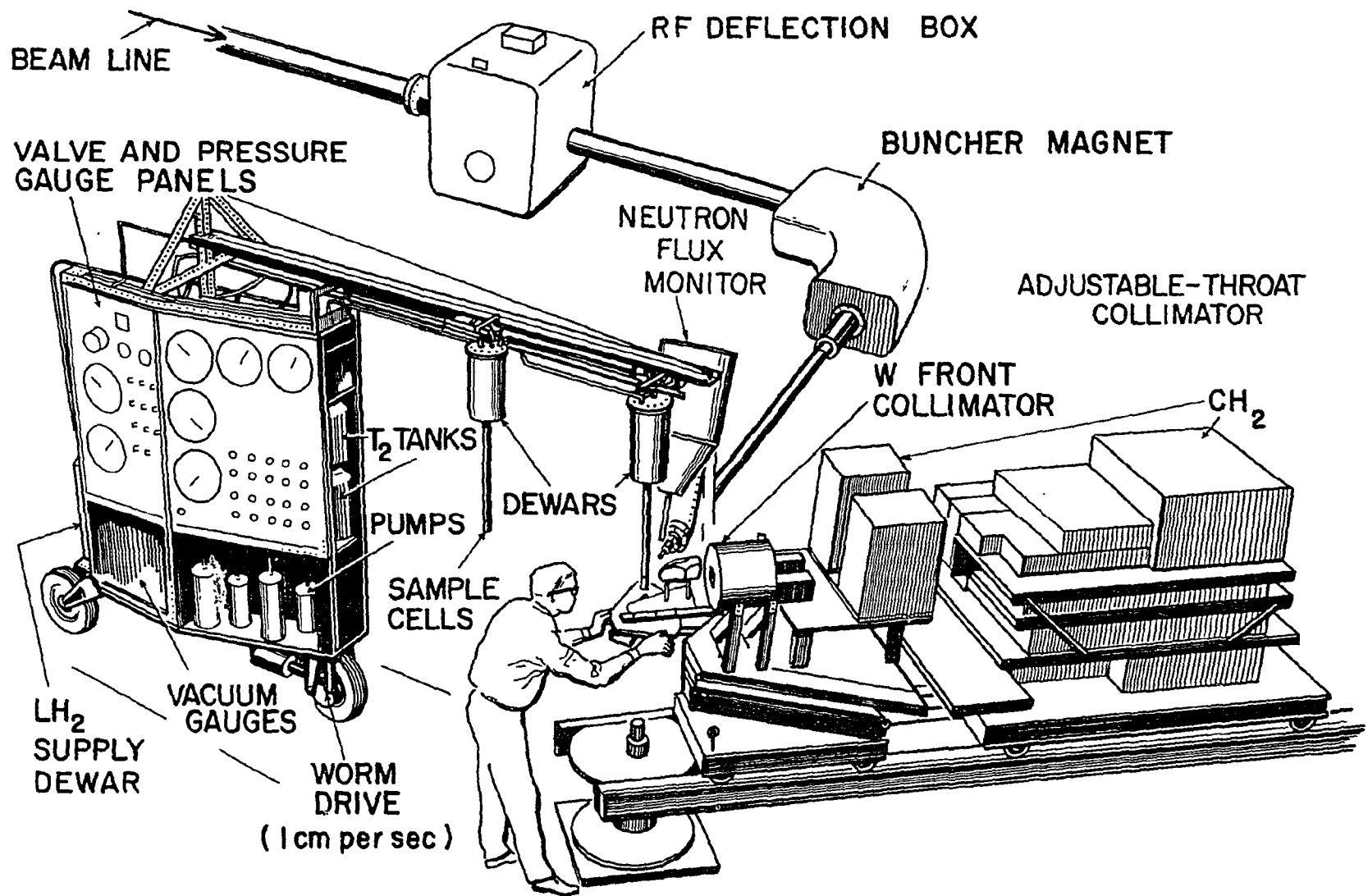


FAST NEUTRON COLLIMATOR ADJUSTABLE THROAT



TIME-OF-FLIGHT APPARATUS  
LIQUID TRITIUM EXPERIMENT

FIG. 9



TIME-OF-FLIGHT APPARATUS (LIQUID TRITIUM EXPERIMENT)

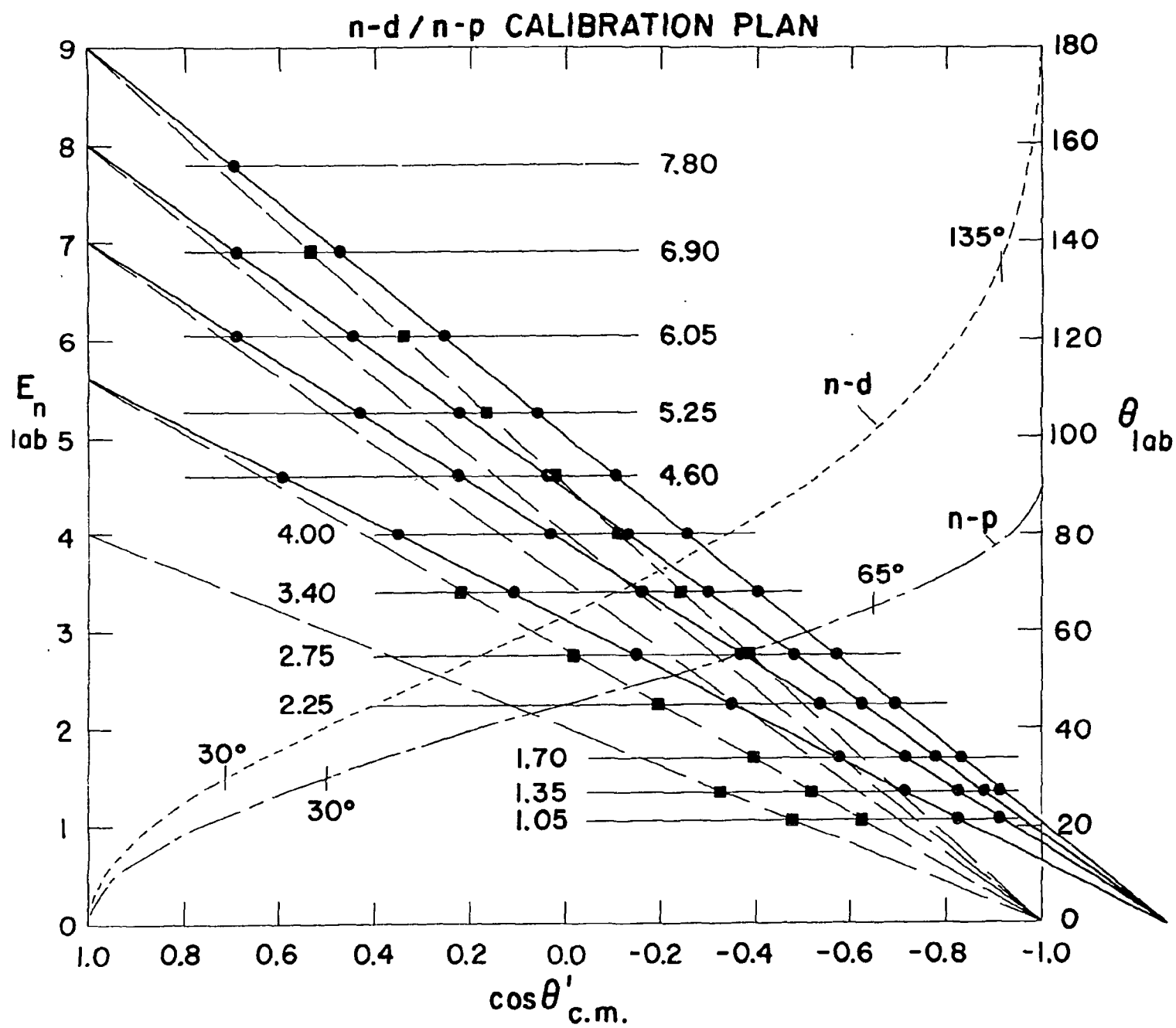


FIG. 11

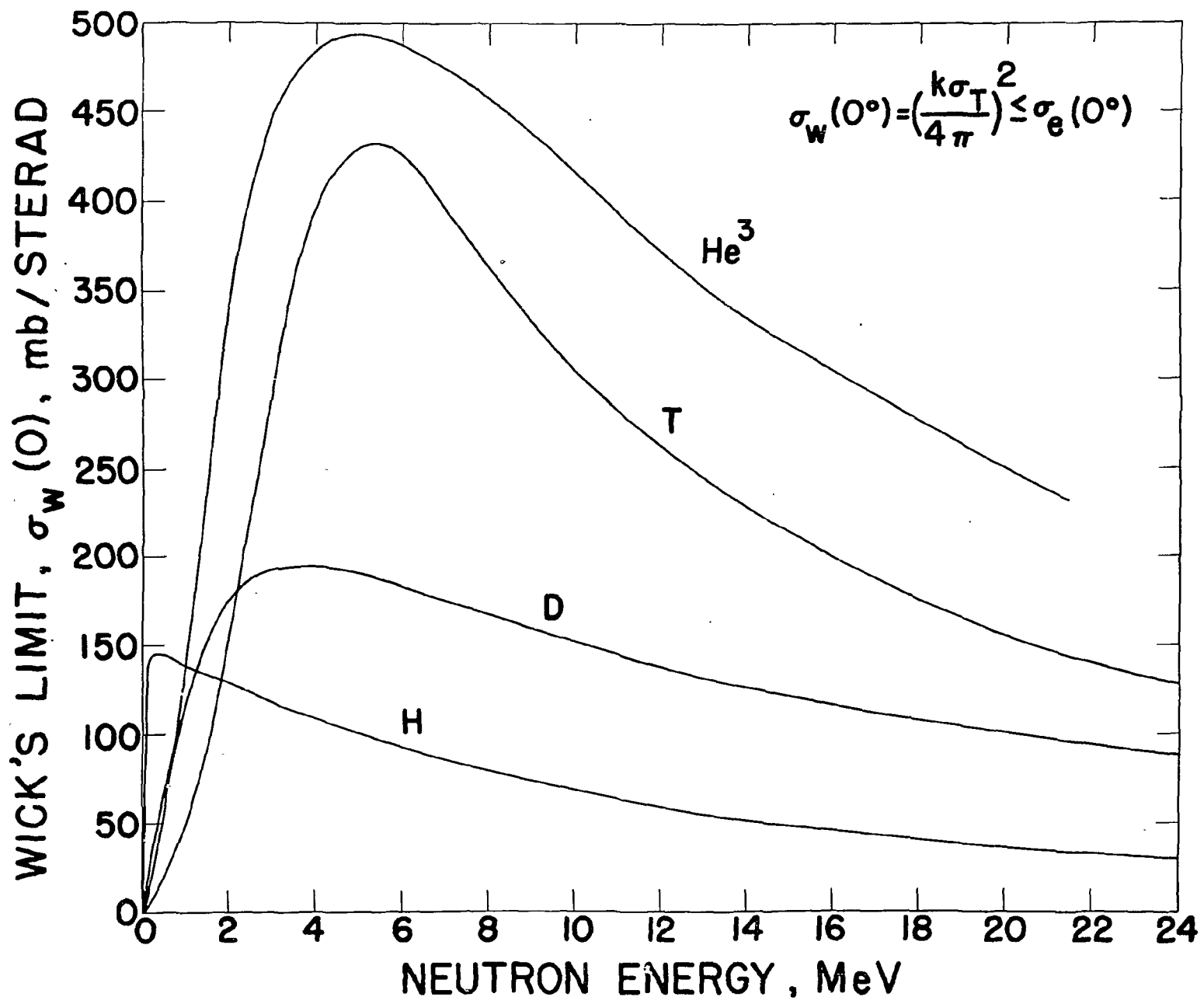


FIG. 12

# NEUTRON ELASTIC SCATTERING FROM DEUTERIUM

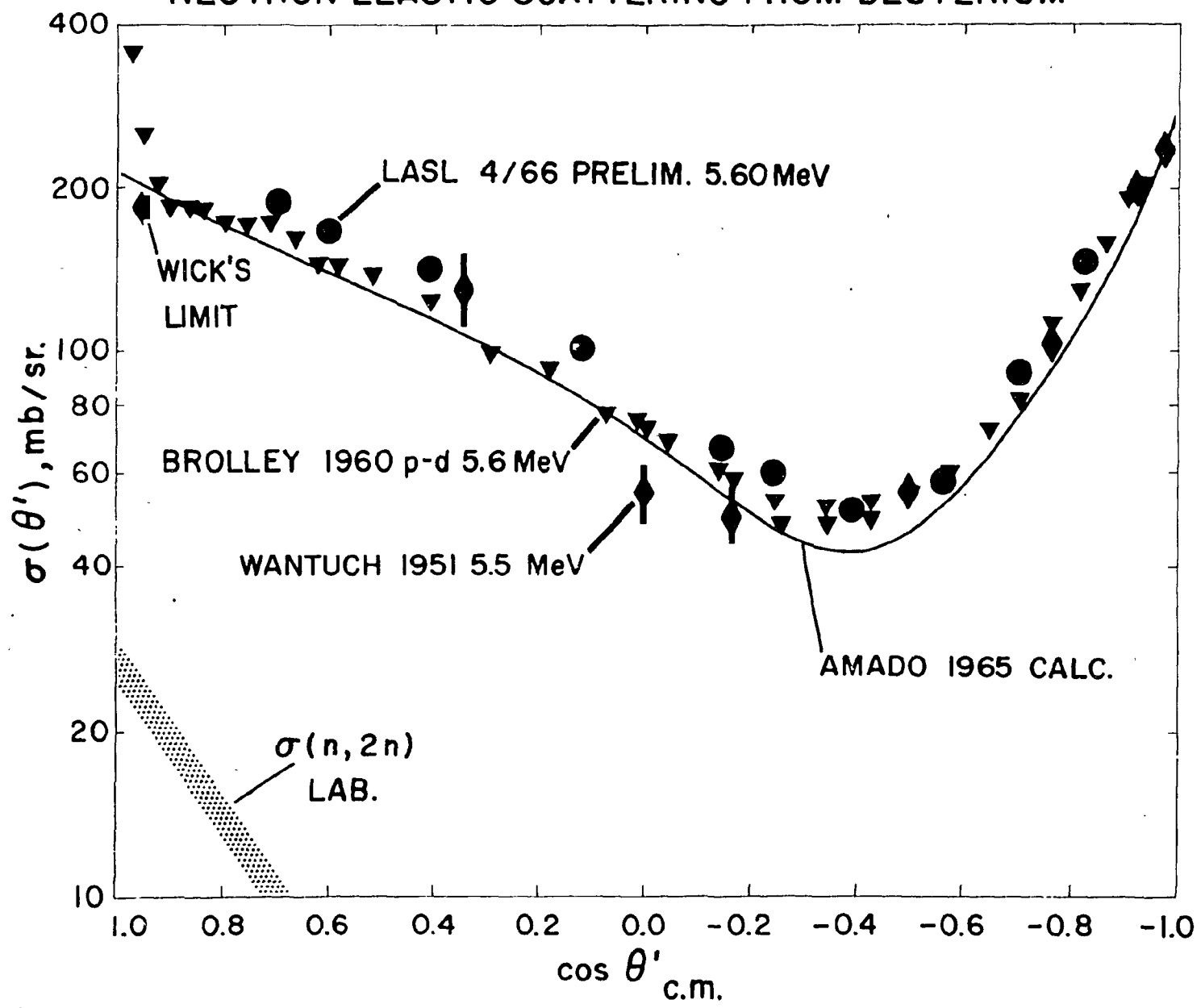


FIG. 13

# NEUTRON ELASTIC SCATTERING FROM DEUTERIUM

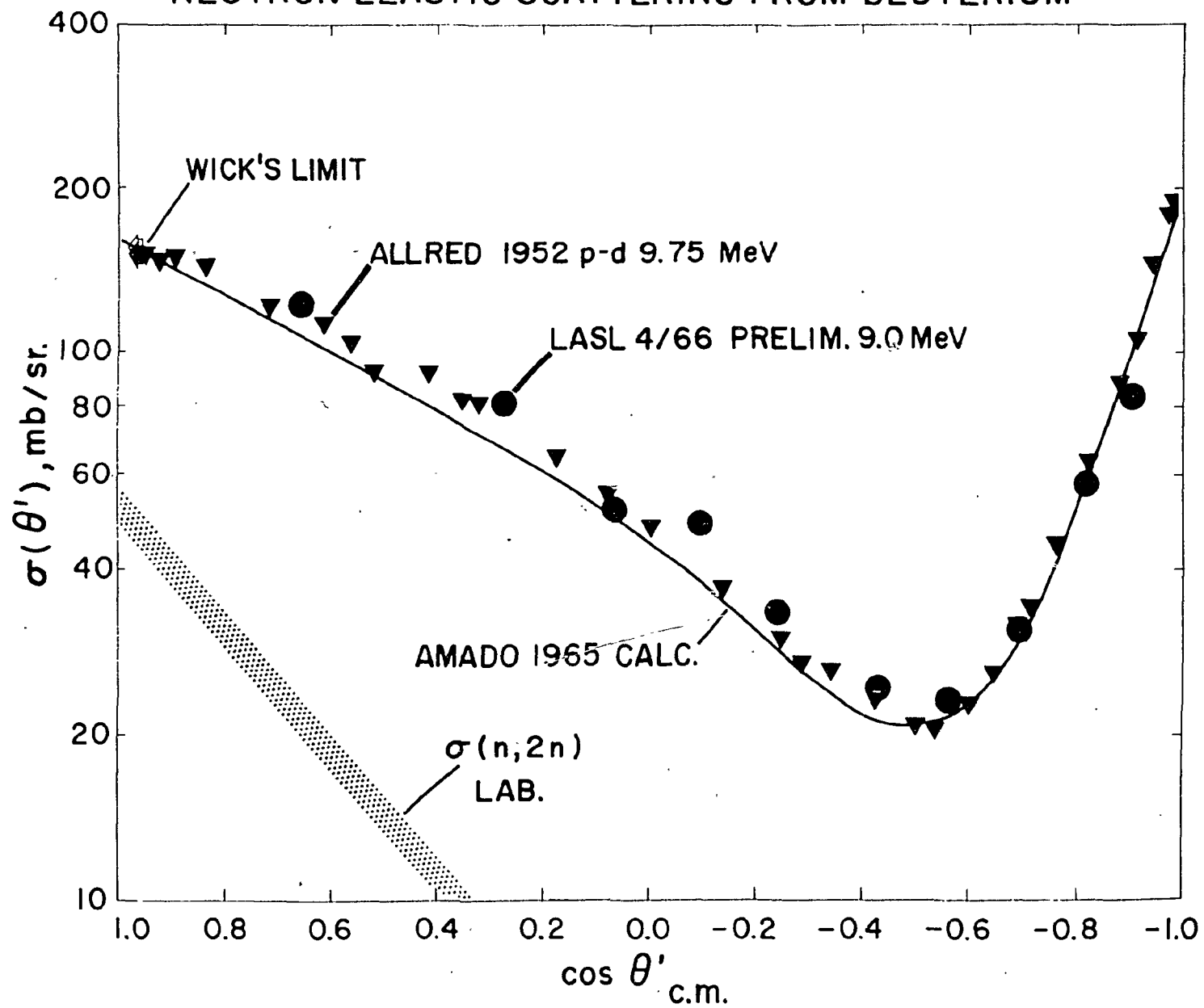


FIG. 14

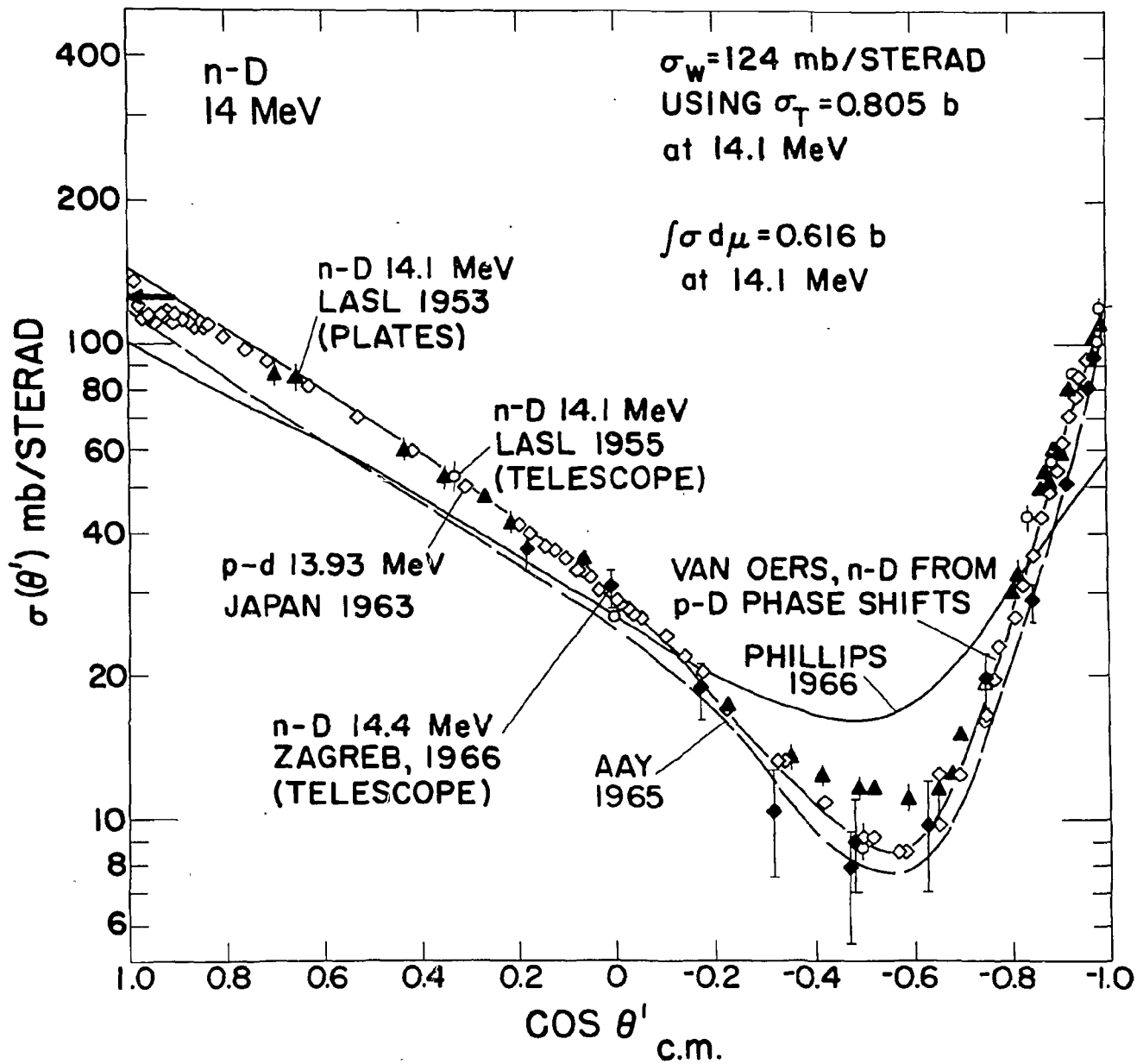


FIG. 15

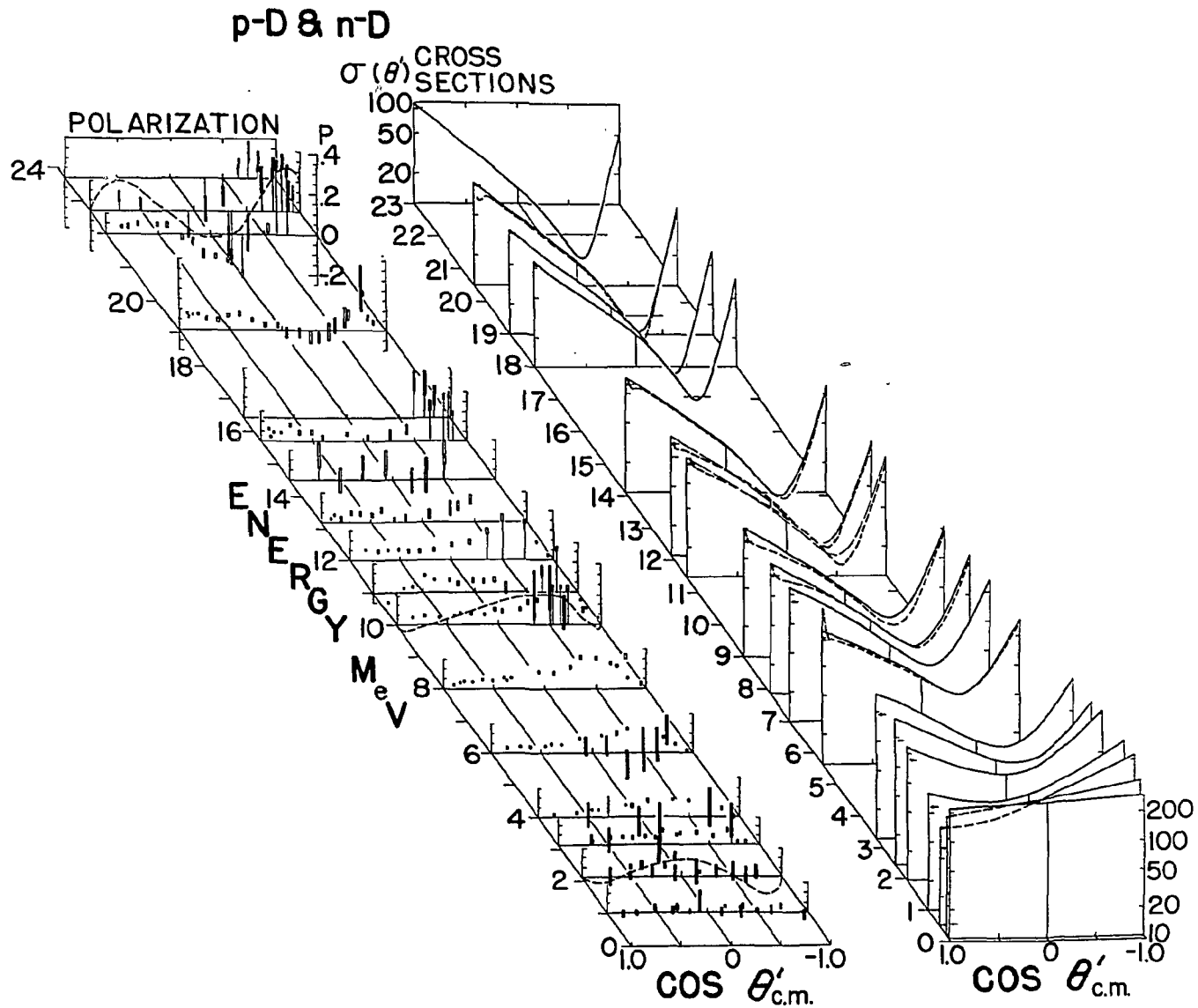


FIG. 16

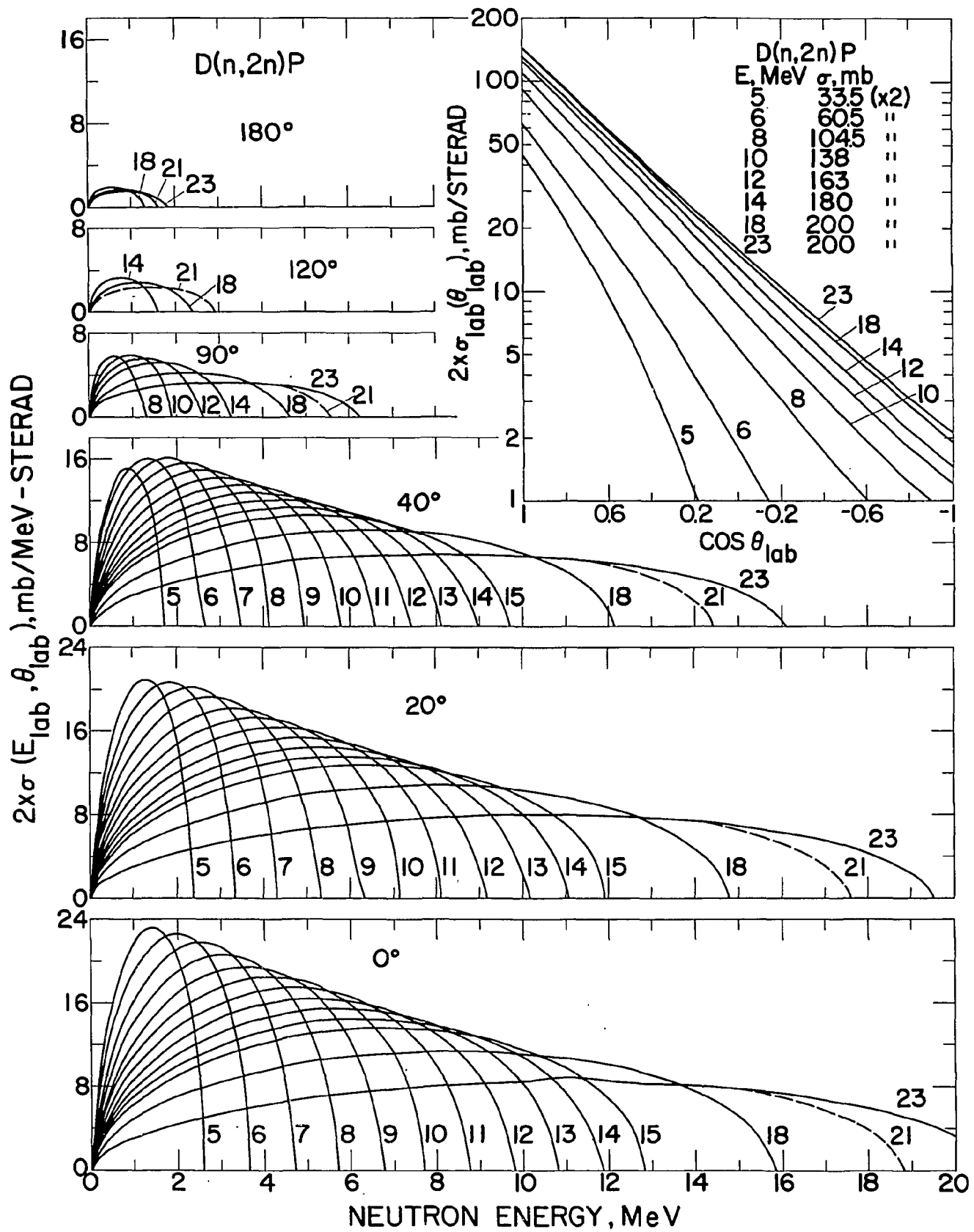


FIG. 17

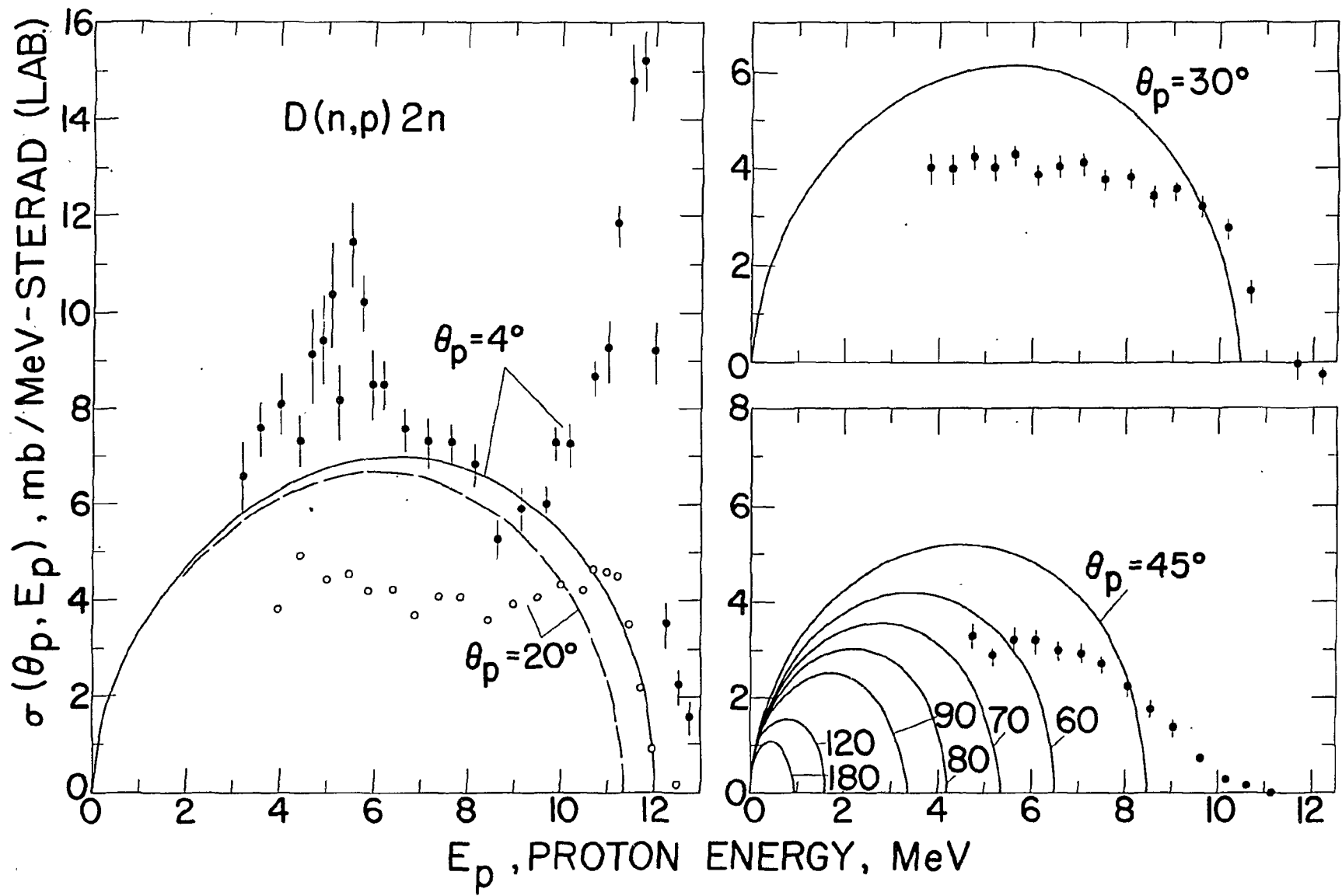


FIG. 18

PROTON SPECTRA FROM D(p,2p)n AT  $E_p = 13.9$  MeV

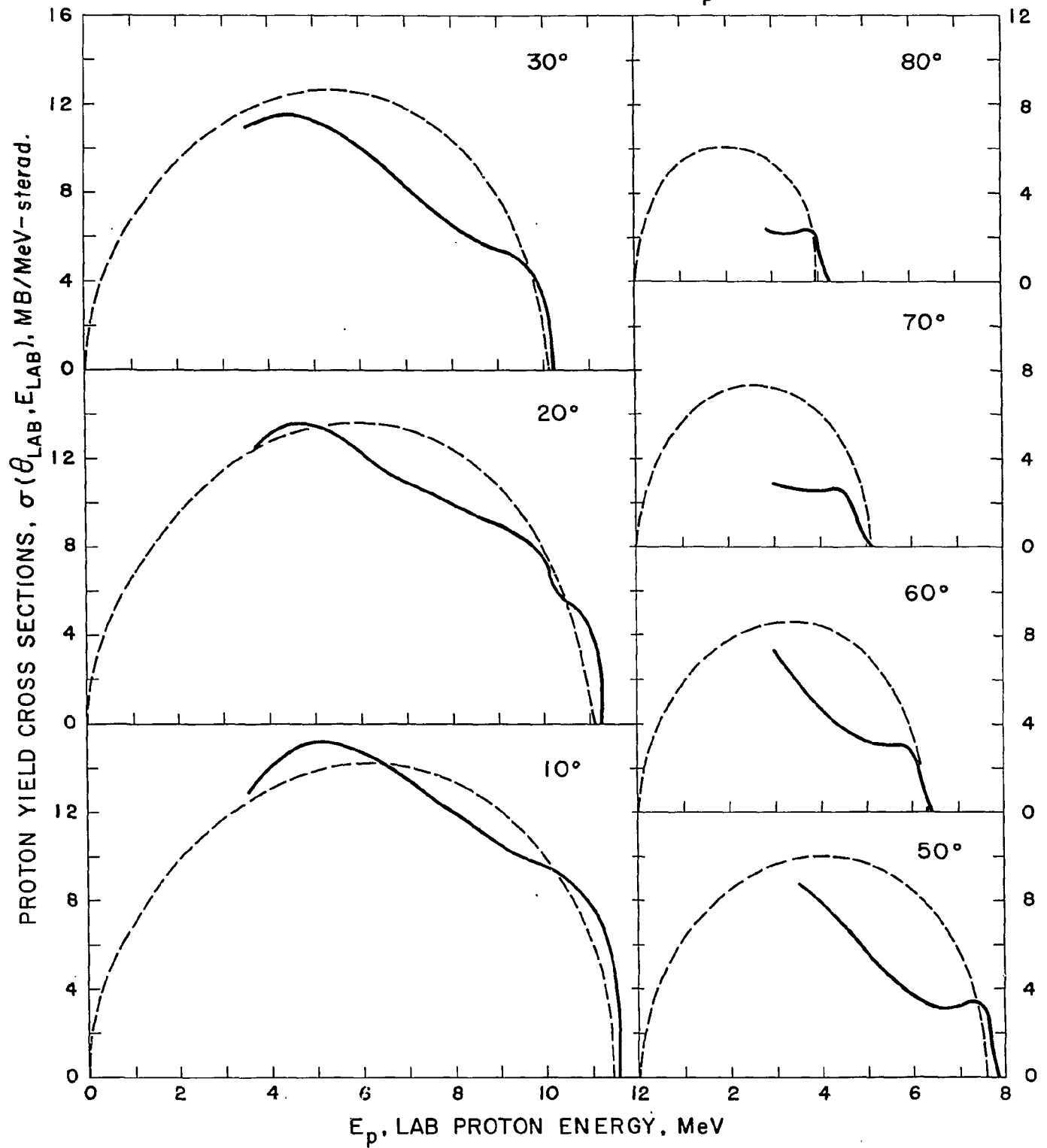


FIG. 19

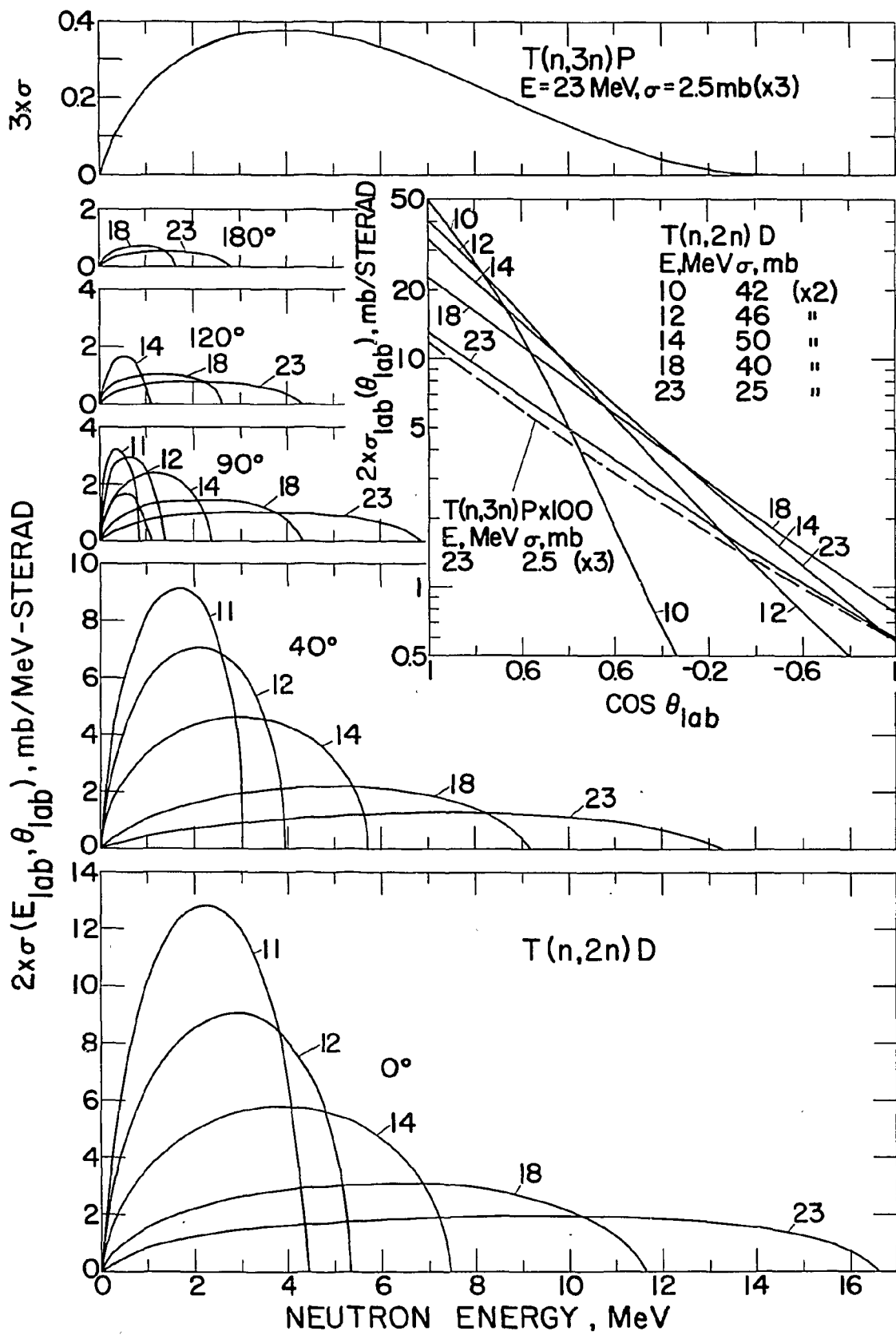


FIG. 20

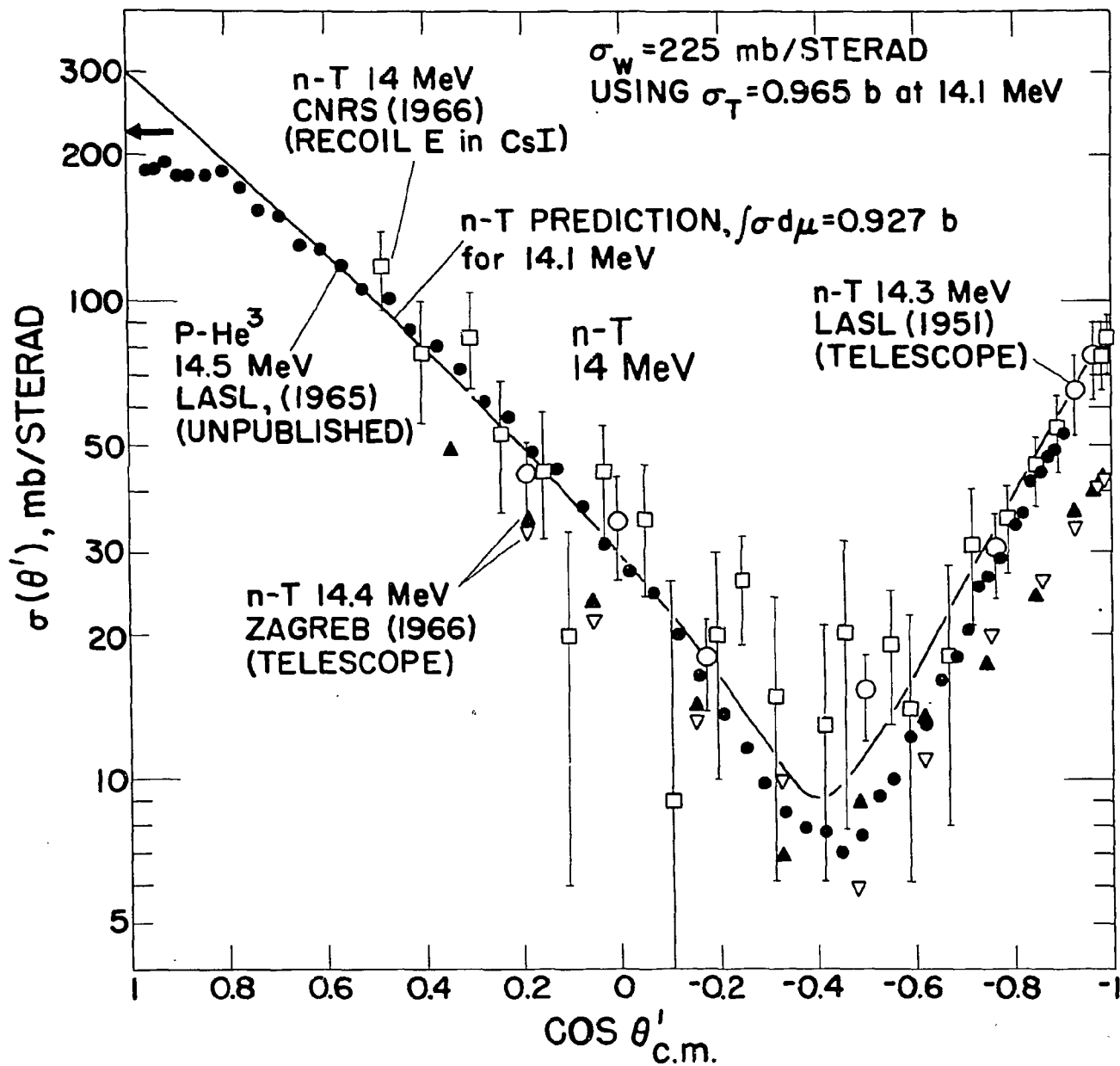


FIG. 21

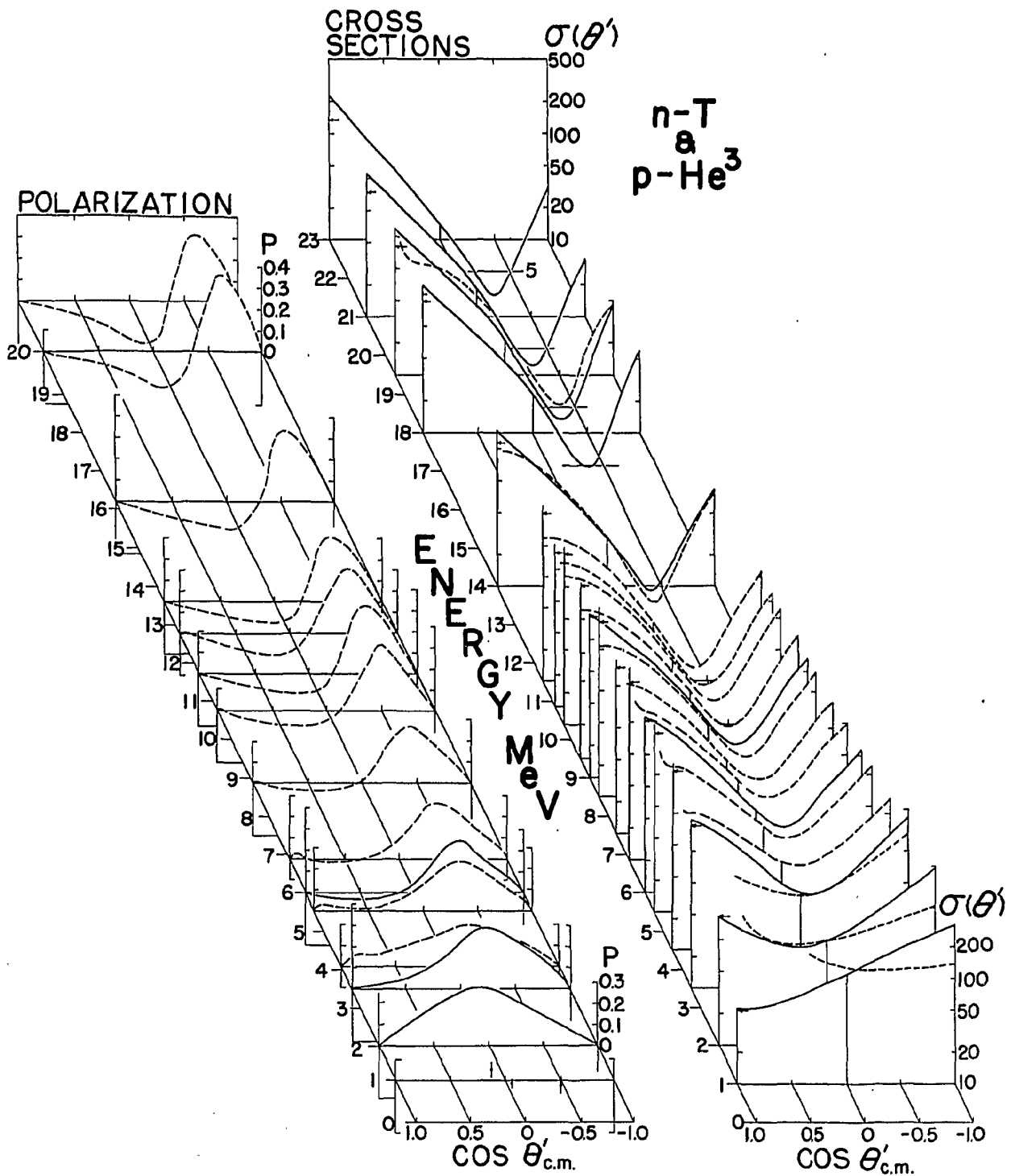


Fig. 22

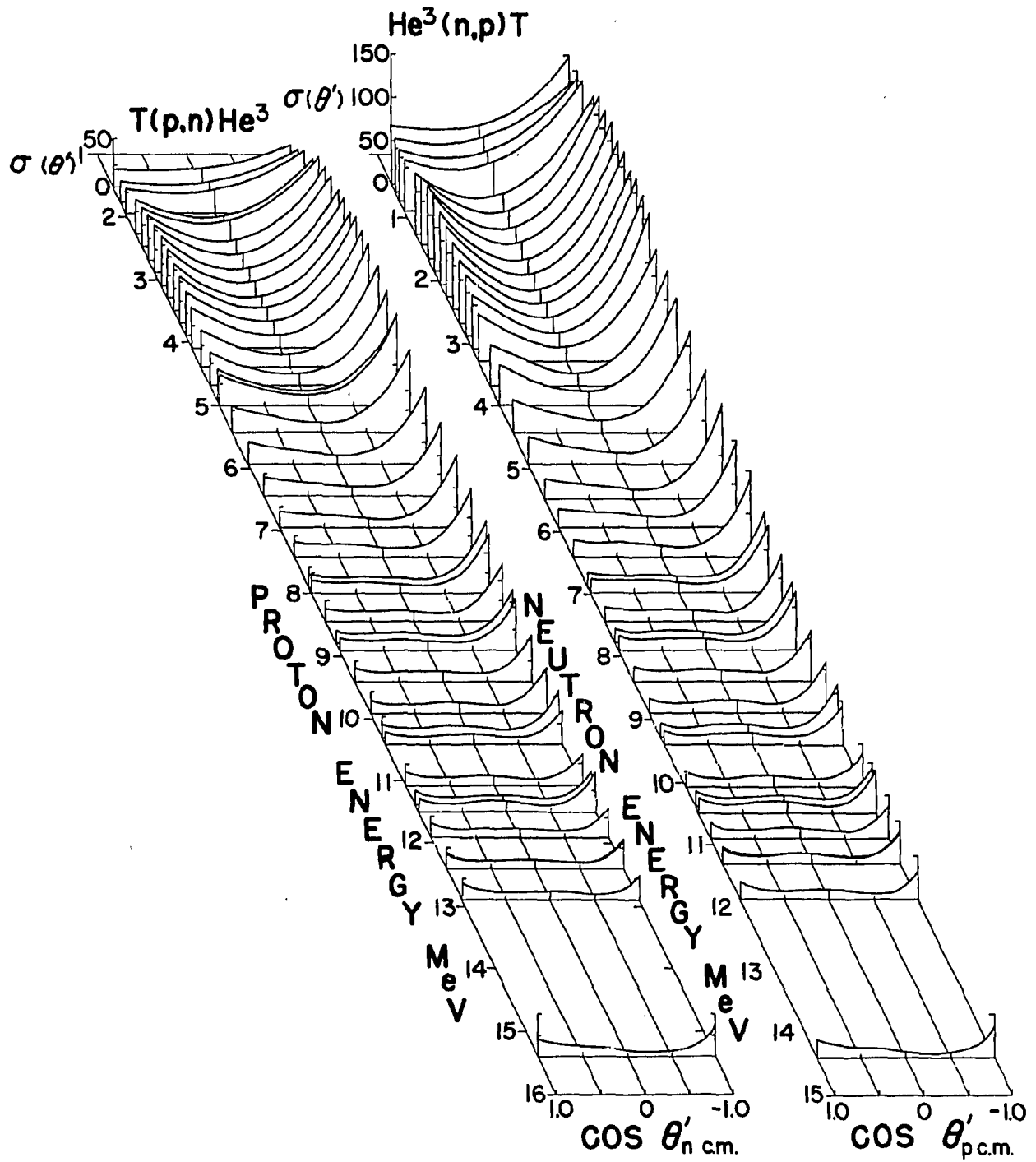


Fig. 23

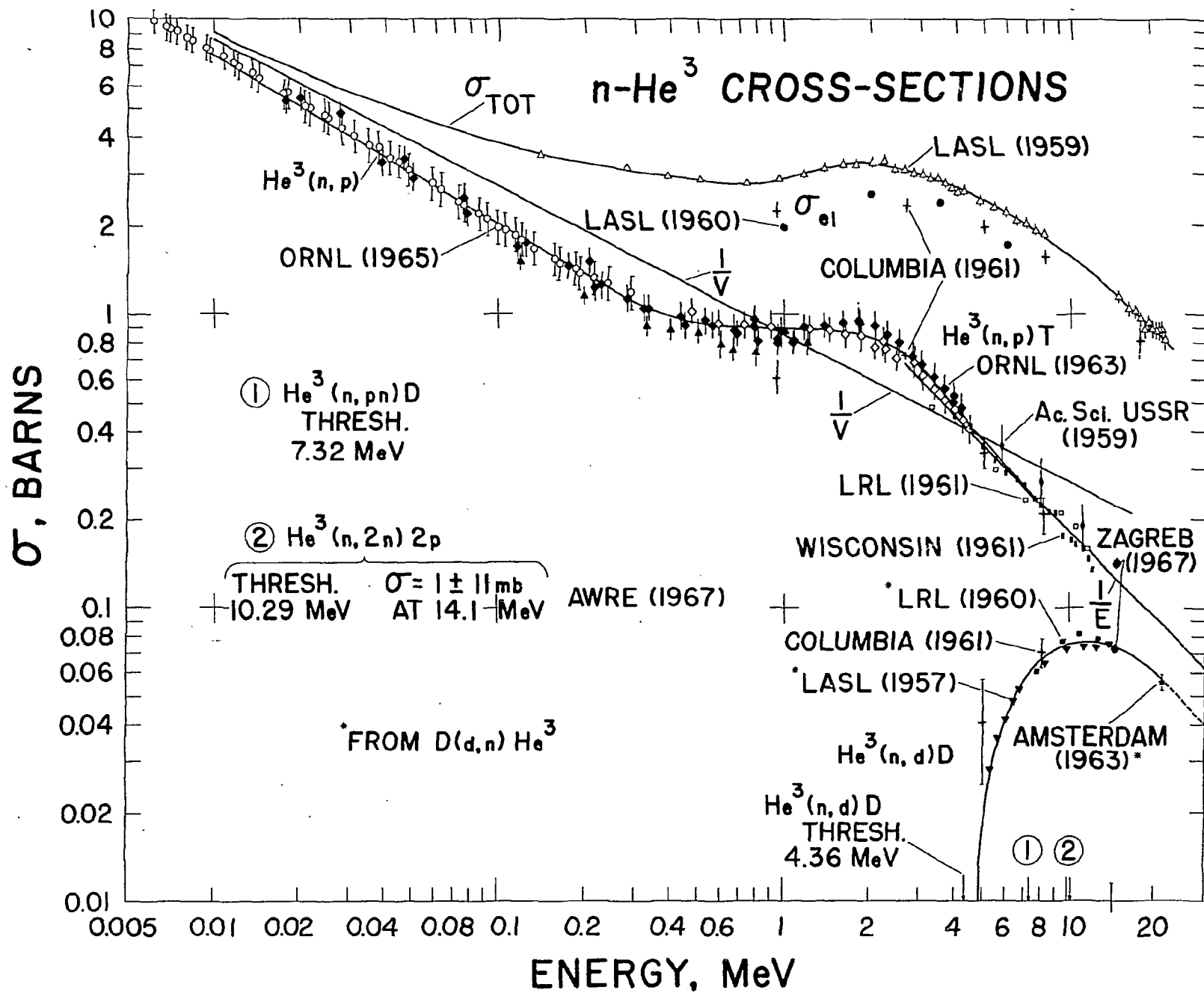


Fig. 24

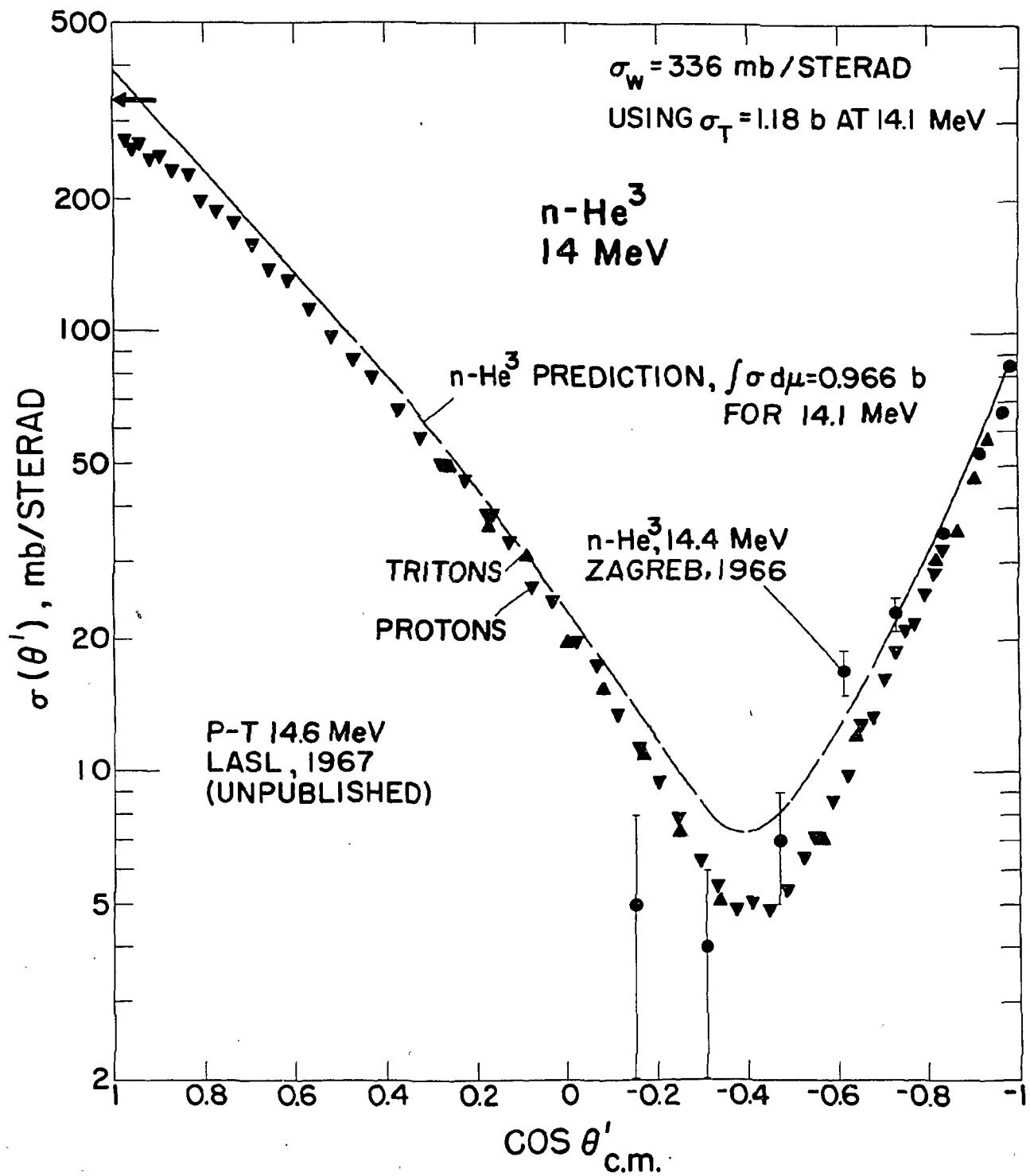


FIG. 25

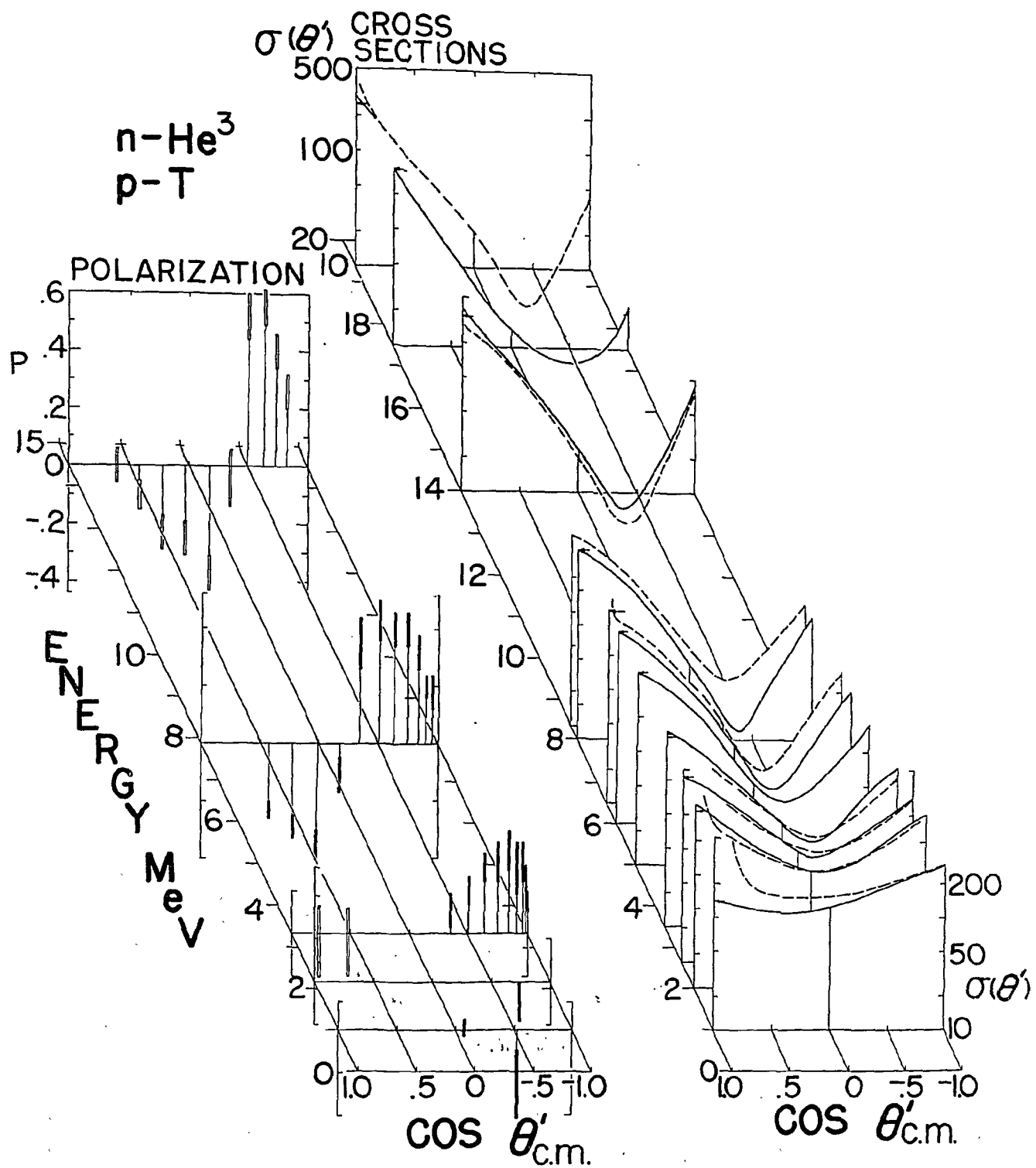


FIG. 26